

1 **Revision 3**

2 **Competitive adsorption geometries for the arsenate As(V) and**
3 **phosphate P(V) oxyanions on magnetite surfaces: Experiments and**
4 **theory**

5 XIAOLIANG LIANG ^{1,6,7}, XIAOJU LIN ^{1,7}, GAOLING WEI ^{2,3}, LINGYA MA ^{1,6,7},
6 HONGPING HE ^{1,6,7*}, DAVID SANTOS-CARBALLAL ^{4*}, JIANXI ZHU ^{1,6,7},
7 RUNLIANG ZHU ^{1,6,7}, NORA H. DE LEEUW ^{4,5}

8 ¹ CAS Key Laboratory of Mineralogy and Metallogeny/Guangdong Provincial Key
9 Laboratory of Mineral Physics and Material Research & Development, Guangzhou
10 Institute of Geochemistry, Chinese Academy of Sciences, Guangzhou 510640, PR
11 China;

12 ² Guangdong Key Laboratory of Integrated Agro-environmental Pollution Control and
13 Management, Guangdong Institute of Eco-environmental Science & Technology,
14 Guangzhou 510650, China;

15 ³ National-Regional Joint Engineering Research Center for Soil Pollution Control and
16 Remediation in South China, Guangzhou 510650, China;

17 ⁴ School of Chemistry, University of Leeds, Leeds LS2 9JT, United Kingdom;

18 ⁵ Department of Earth Sciences, Utrecht University, Princetonplein 8A, 3584 CD
19 Utrecht, The Netherlands;

20 ⁶ Institutions of Earth Science, University of Chinese Academy of Sciences, Beijing
21 100049, P.R. China;

22 ⁷ University of Chinese Academy of Sciences, Beijing 100049, PR China.

*Corresponding author. E-mail: hehp@gig.ac.cn (H.P. HE);

D.Santos-Carballal@leeds.ac.uk (D. Santos-Carballal).

23

ABSTRACT

24 In the present study, the competitive adsorption geometries for arsenate and phosphate
25 on magnetite surfaces over a pH range of 4-9 was investigated using *in situ* attenuated
26 total reflectance Fourier-transform infrared spectroscopy (ATR-FTIR) and
27 two-dimensional correlation analysis (2D-COS). The adsorption energies and infrared
28 vibrational frequencies of these surface complexes were also calculated by first
29 principles simulations. Arsenate and phosphate have different preferences for the
30 magnetite surface in the presence of aqueous solvent at both acid and alkaline pH. For
31 the adsorption of phosphate, mono-protonated monodentate mononuclear (MMM)
32 complexes dominated at acid pH, while non-protonated bidentate binuclear (NBB)
33 complexes were dominant at alkaline pH. Arsenate mainly formed bidentate binuclear
34 (BB) complexes with some outer-sphere species, both of which were more prevalent
35 at acid pH. The pre-absorbed inner-sphere arsenate species were scarcely affected by
36 the introduction of phosphate. However, the pre-absorbed phosphate oxyanions,
37 especially the MMM complexes, were significantly substituted by BB arsenate at the
38 magnetite surfaces. The adsorption affinity of phosphate and arsenate species for
39 magnetite surface was found to increase in the following order: MMM phosphate
40 complex < NBB phosphate complex < BB arsenate complex, which was consistent
41 with the calculated adsorption energies. The simulated infrared vibrational
42 frequencies for the most favored adsorption modes of each oxyanion display
43 distinctive patterns, in which trends are in excellent agreement with experimental
44 data.

45 The effects of pH, adsorption sequence and mineral species on the competitive
46 adsorption between arsenate and phosphate oxyanions are also discussed, and their
47 different competing ability and stability on the magnetite surfaces were ascribed to the
48 variations in adsorption geometry and strength of binding. To the best of our
49 knowledge, this is the first study aiming to distinguish the stability of the different
50 phosphate and arsenate complexes on magnetite by employing a highly suitable
51 combination of powerful *in situ* spectroscopy and DFT simulations.

52 This study provides molecular-level insight into the geometries and relative stabilities
53 of the adsorption of phosphate and arsenate on magnetite surfaces, which is useful for
54 the interpretation of the mobility and bioavailability of these anions.

55 **Keywords:** Phosphate; Arsenate; Competitive adsorption; Adsorption geometry;
56 ATR-FTIR; First-principles simulations

INTRODUCTION

57

58 Contamination of soil and aquatic systems by arsenic (As) and phosphorus (P) is of
59 global environmental concern. Arsenic is often found at elevated concentrations in
60 freshwater, attributed to a variety of natural (e.g., geothermal processes and mineral
61 weathering) and anthropogenic (e.g., mining industry and agriculture) processes
62 (Kocourkova-Vikova et al., 2015; Kunhikrishnan et al., 2017). Owing to its
63 biotoxicity and carcinogenic risk, the presence of arsenic in drinking water ranks
64 among the greatest threat to public health (Antelo et al., 2015), which has led the
65 World Health Organization to propose a limit of $10 \mu\text{g L}^{-1}$ (WHO, 2011). However, in
66 the arsenic contaminated water, the As concentration can reach several ppm
67 (Chakraborti et al., 2002; Sprague and Vermaire, 2018; Winkel et al., 2011). Arsenic
68 exists in several oxidation states (-III, 0, III and V), with arsenate (AsO_4^{3-}) being the
69 most common form found in natural aqueous systems (Choppala et al., 2016).
70 Phosphorous (P) is an essential nutrient for plant growth. But the input of excess P
71 from agricultural land runoff or over-fertilization may lead to levels above the limit of
72 0.1 mg L^{-1} recommended by the United States Environmental Protection Agency
73 (USEPA), causing severe environmental problems including eutrophication (Neupane
74 et al., 2014). P occurs naturally only in the pentavalent state, forming
75 ortho-phosphates, pyrophosphates, longer-chain polyphosphates and several types of
76 organic phosphates (Correll, 1998).
77 After their release from natural and anthropogenic sources, As and P undergo a series
78 of geochemical reactions, e.g., adsorption, reduction/oxidation, precipitation (Zhang

79 et al., 2017b), and sequestration by soil and sediments (Grossl et al., 1997). The
80 adsorption in the mineral/water interface is vital for their mobility. Iron (hydr)oxides
81 are ubiquitous in soils and aquatic sediments (Pedersen et al., 2005), with high
82 adsorption affinity towards arsenate and phosphate. The surface complexation is the
83 dominant adsorption mechanism reported for arsenate and phosphate species, as
84 verified in macroscopic batch experiments (Swedlund et al., 2014), model
85 calculations (Tiberg et al., 2013) and microscopic studies (Johnston and Chrysochoou,
86 2014). Bidentate-binuclear (BB), monodentate-mononuclear (MM) and
87 bidentate-mononuclear (BM) complexes are the prevalent surface binding
88 configurations of arsenate and phosphate on iron oxides (Fendorf et al., 1997; Liu et
89 al., 2015), with distribution dependent on pH, ionic strength, and surface coverage
90 (Krumina et al., 2016). Generally, the ability to form bridging bidentate surface
91 complexes is dependent upon the proximity of terminal Fe-O sites on the surface (Livi
92 et al., 2017; Villalobos et al., 2009).

93 P and As belong to group 5A of the periodic table and form species with comparable
94 chemical properties. Both arsenate and phosphate oxyanions have a tetrahedral
95 geometry with close thermochemical radii, i.e., 2.48 and 2.38 Å (Silva and Fraustoda,
96 2001), respectively, and very similar proton affinities, e.g., 2.2, 7.0 and 11.5 for pK_{a1} ,
97 pK_{a2} and pK_{a3} of arsenate and 2.2, 7.2 and 12.3 for pK_{a1} , pK_{a2} and pK_{a3} of phosphate
98 (Elzinga and Sparks, 2007; Mohan and Pittman, 2007). Thus, they display analogous
99 adsorption characteristics in the aspects of kinetics, pH dependence, and effect of
100 ionic strength. As arsenate and phosphate oxyanions frequently occur together in

101 surface environments, their competitive adsorption onto mineral surfaces explicitly
102 determines their bioavailability and leachability, which is crucial for the prediction of
103 potential risk of environmental contamination. However, the current knowledge on
104 this hypothesis is scattered and fragmented, even regarding the adverse effect of
105 phosphate on arsenate adsorption. For example, arsenate is found preferentially
106 adsorbed on iron oxide at a low pH, whereas phosphate shows the opposite trend (Han
107 and Ro, 2018). But in soil stabilized by iron oxide, phosphate can replace the
108 adsorbed arsenate when the concentration of the former is larger than the latter (So et
109 al., 2012). This is contrary to the results reported by Hashem et al., where arsenate
110 was found bonded to iron oxide more strongly than phosphate (Hashem et al., 2015).
111 Moreover, contradictory information is also found in the literature concerning the
112 adsorption geometry. For arsenate, BB complexes were considered as the predominant
113 adsorption configuration on iron oxide surfaces (Carabante et al., 2010). MM
114 coordination is also found for arsenate binding on some iron oxides, as verified by
115 combined EXAFS and IR analyses (Antelo et al., 2015; Loring et al., 2009). Although
116 BM configuration has also been assigned under certain conditions (Neupane et al.,
117 2014), these have been excluded by Sherman et al., as the EXAFS signal attributed to
118 the BM complex was simply due to multiple scattering (Sherman and Randall, 2003).
119 For phosphate, the IR analysis indicates that protonated BB complexes are the
120 predominant species on iron oxides at pH between 3 and 6, whereas the
121 non-protonated BB complexes are dominant at $\text{pH} > 7.5$ (Carabante et al., 2010). On
122 the contrary, the surface complexation modeling (SCM) predicts that deprotonated BB

123 phosphate and deprotonated MM phosphate dominate at lower pH and higher pH
124 values, respectively, while the contribution of protonated BB is very small
125 (Kanematsu et al., 2010). This shows ~~that~~ great divergence in the competitiveness
126 ~~exists~~ not only within the individual adsorption geometries of phosphate and arsenate,
127 but also during their co-adsorption.

128 To date, the competitive adsorption of arsenate and phosphate on calcite (So et al.,
129 2012), clay minerals (Violante and Pigna, 2002), and certain iron oxides, e.g.,
130 ferrihydrite (Antelo et al., 2015) and goethite (Zhao and Stanforth, 2001), has been
131 investigated intensively. In comparison, their competitive adsorption on magnetite,
132 which is a common constituent of soil and sediment, is poorly understood. Magnetite
133 exists in anoxic sediments and soils (Guo and Barnard, 2013), and is formed naturally
134 via several pathways, including ferrous iron oxidation and iron metal corrosion, as
135 well as chemical and biological reduction of ferric oxides (Gorski et al., 2010).
136 Additionally, the remediation of contaminated groundwater and soil is increasingly
137 carried out using an emerging technology based on zero-valent iron (ZVI)
138 nanoparticles, where magnetite is the major corrosion product formed as the outer
139 layer of ZVI (Filip et al., 2014). With the inverse spinel structure, magnetite has
140 several features that make its reaction properties interesting; specifically, (i) electron
141 donor Fe^{2+} ions on octahedral sites, which are active for the reduction of certain
142 oxyanions, e.g., CrO_4^{2-} and UO_3^- ; and (ii) octahedral Fe^{2+} and Fe^{3+} cations which can
143 oxidize and reduce reversibly during the reaction with adsorbed oxyanions, while
144 keeping the spinel structure unaffected. In previous studies, magnetite is shown to be

145 efficient at scavenging metal oxyanions in natural and engineered aquatic systems,
146 including chromate (Zhang et al., 2017a), arsenate (Zhang et al., 2011), and uranyl
147 (Scott et al., 2005). These properties and behavior highlight the important role of
148 magnetite in the transport of arsenate and phosphate in soil and aqueous systems. Due
149 to the low specific surface area or surface site density of magnetite ($<50 \text{ m}^2 \text{ g}^{-1}$, 1–2
150 sites nm^{-2}) (Sun et al., 1998; Tamura et al., 1993), relative to ferrihydrite ($>200 \text{ m}^2 \text{ g}^{-1}$,
151 2.5–3 sites nm^{-2}) (Hiemstra, 2013) and goethite ($<50 \text{ m}^2 \text{ g}^{-1}$, 2.5–3.5 sites nm^{-2})
152 (Ona-Nguema et al., 2005; Zhao and Stanforth, 2001), the resulting low surface
153 coverage of arsenate and phosphate on magnetite makes it difficult to analyze
154 spectroscopically. Extended X-ray absorption fine structure (EXAFS) spectroscopy is
155 the most widespread technique used to investigate the geometry of surface complexes
156 (Ona-Nguema et al., 2005), which has shown the formation of BB arsenate complexes
157 on the surfaces of ferrihydrite, hematite, goethite and lepidocrocite (Sherman and
158 Randall, 2003). However, it is difficult to analyze light elements such as P using soft
159 X-rays, due to their poor signal-to-noise ratios. *In situ* attenuated total reflectance
160 Fourier-transform infrared (ATR-FTIR) spectroscopy is a reliable method that is
161 capable of tracing the coordination environment and protonation state of most
162 oxyanions at mineral-water interfaces without interference of signals from the liquid
163 phase (Brechtbuhl et al., 2012). Although the in individual and competitive
164 coordination structure of phosphate and arsenate on ferrihydrite, goethite and hematite
165 has been previously investigated using ATR-FTIR, the analysis of the relatively broad
166 vibrational bands led to inconclusive interpretation (Gao et al., 2013). Recently,

167 two-dimensional correlation spectroscopy (2D-COS) has been successfully applied in
168 ATR-FTIR analysis by resolving overlapped peaks and enhancing the spectral
169 resolution (Yan et al., 2016). Despite the advances achieved using ATR-FTIR in the
170 understanding of the adsorption mechanism and geometries of phosphate and arsenate
171 complexes, it is still unclear what are the factors that drive their competition under
172 complex and realistic conditions. This uncertainty may be resolved by employing
173 periodic density functional theory (DFT) calculations and comparing the simulated
174 geometries, vibrational modes, and/or relative adsorption energies to experimental
175 results, which will provide a better understanding from a thermodynamic point of
176 view of the competition between arsenate and phosphate (He et al., 2009).

177 In this study, the competitive adsorption of arsenate and phosphate species on the
178 surface of chromium-doped magnetite was investigated by *in situ* ATR-FTIR
179 spectroscopy and complemented by DFT calculations. An interesting feature of
180 natural magnetite is the substitution of iron by other metals, while maintaining the
181 spinel structure. Cr is the a common impurity element in natural magnetite as trace
182 element (less than 0.1%), minor element (0.1%-1%) and major element (more than
183 1%), forming solid solution series between magnetite (Fe_3O_4) and chromite (FeCr_2O_4)
184 (Dupuis and Beaudoin, 2011). Moreover, the substitution of Cr^{3+} for Fe^{3+} is known to
185 enhance the adsorption capacity of magnetite (Liang et al., 2012), and thus increase
186 the signals and accuracy of *in situ* ATR-FTIR experiments. The competitive
187 adsorption was carried out under different addition subsequences. A discussion and
188 comparison between our results and previous investigations was also conducted and a

189 comprehensive atomic-level understanding on the adsorption of phosphate and
190 arsenate on magnetite is used to better interpret their geochemical behaviors in the
191 earth surface and their effects on nucleation, growth, and phase transformation of the
192 mineral phases.

193

194 **MATERIALS AND METHODS**

195 **Preparation of Cr-substituted magnetite**

196 Magnetite with Cr substitution was synthesized by the precipitation-oxidation method
197 described in Text A.1. The obtained sample had the spinel structure (Figure. A.1) and
198 X-ray absorption fine structure (XAFS) spectra illustrated that chromium in the
199 valence state of +3 mainly occupies the octahedral sites. The detailed discussion of
200 XAFS results has been presented elsewhere (Liang et al., 2013). The high surface area
201 ($112 \text{ m}^2 \text{ g}^{-1}$) and surface site density ($3.6 \text{ sites nm}^{-2}$) of the magnetite particles (Table
202 A.1) increased the likelihood of obtaining good contact and allowed us to probe large
203 quantities of adsorbed species (Liang et al., 2017). During the adsorption, the
204 concentration of leaching Cr and Fe was below the detection limit of the instrument.

205

206 ***In situ* ATR-FTIR and 2D-COS analyses**

207 *In situ* ATR-FTIR analysis of phosphate and arsenate adsorption on magnetite was
208 conducted using a Bruker Vertex 70 FTIR spectrometer equipped with a liquid
209 N_2 -cooled MCT detector and a horizontal ATR accessory made of ZnSe crystal.
210 Before the IR analysis, the magnetite particle layer was prepared on the ZnSe crystal.

211 1 mL of magnetite suspension (5 g L^{-1}) was dropped onto the crystal surface and dried
212 overnight at room temperature. The film was then rinsed with deionized (DI) water to
213 remove the loosely deposited particles, which stabilized the deposited layer (Hug,
214 1997). At the end of adsorption experiment, the magnetite film was inspected for
215 signs of film erosion, which were not observed.

216 Before adsorption, a NaCl background electrolyte solution (0.01 mol L^{-1}) at the
217 designated pH was flowed through the cell with magnetite deposition layer at a rate of
218 1 mL min^{-1} until no further change in spectra was seen. A background spectrum
219 comprising the absorbance of the ZnSe crystal and the deposited adsorbent was then
220 collected, followed by the injection of solutions containing $100 \text{ } \mu\text{mol L}^{-1}$ of arsenate
221 or phosphate, and 0.01 mol L^{-1} of NaCl to start the adsorption reaction. IR spectra
222 were recorded as a function of time until the adsorption reached equilibrium without
223 any signal variation. NaCl was selected as the background electrolyte, because it was
224 inert or non-adsorbed on solid surfaces. All liquid samples were purged with N_2
225 during spectrum collection. The pH was adjusted within the range of 4.0–9.0 using
226 NaOH (0.1 mol L^{-1}) and HCl (0.1 mol L^{-1}). Desorption experiments were conducted
227 by introducing NaCl solution (0.01 mol L^{-1}) into the ZnSe cell when the adsorption of
228 oxyanions reached equilibrium. The comparative adsorption was carried out through
229 the reversible substitution of arsenate solution ($100 \text{ } \mu\text{mol L}^{-1}$ at pH 4.0 and 7.0, and
230 $500 \text{ } \mu\text{mol L}^{-1}$ at pH 9.0) with phosphate solution of the same concentration. It is
231 necessary to emphasize that the arsenate concentrations used in this study, i.e., 100
232 and 500 ppm are at the low end of the range of concentrations examined in past

233 experimental studies (molecular-scale studies: 5 to 10000 $\mu\text{mol L}^{-1}$, macroscopic
234 studies: 0.7 to 30000 $\mu\text{mol L}^{-1}$), as indicated by Catalano, et al. (Catalano et al., 2008).
235 The IR spectra were processed and analyzed with the OPUS software. Curve-fitting
236 analysis of the peaks was conducted using the Gaussian line shape. To obtain an
237 accurate assignment of the IR peaks for the surface complexes, the spectra were
238 analyzed using the 2D-COS technique (Text A.2).

239

240 **Computational methods**

241 To simulate the interaction between the $\text{Fe}_3\text{O}_4(001)$ surface and phosphate/arsenate
242 oxyanions in aqueous solution, the periodic plane-wave density functional theory
243 (DFT) method within the Vienna *ab-initio* simulation package (VASP) was employed
244 (Kresse and Furthmuller, 1996a; Kresse and Furthmuller, 1996b; Kresse and Hafner,
245 1993; Kresse and Hafner, 1994). The Perdew, Burke and Ernzerhof (PBE) semi-local
246 functional approximation was used to calculate the exchange-correlation energy
247 (Perdew et al., 1996; Perdew et al., 1997). The projector augmented wave (PAW)
248 method was used to model the atomic frozen core states and their interaction with the
249 valence levels (Fe: $4d5s$, O: $2s2p$, H: $1s$, P: $3s3p$ and As: $4s4p$) (Blochl, 1994; Kresse
250 and Joubert, 1999). The expansion of the Kohn-Sham (KS) valence states was
251 calculated with a kinetic energy cut-off of 400 eV. We have tested larger cut-off values,
252 but these led to negligible energy differences with respect to a reference, such as the
253 adsorption energies reported in our previous studies (Santos-Carballal et al., 2018;
254 Santos-Carballal et al., 2014). The electronic partial occupancies were determined

255 during geometry optimizations using the Gaussian smearing method with the width
256 set at 0.02 eV (Mermin, 1965). Furthermore, the tetrahedron method with Blöchl
257 corrections was used in static simulations to obtain accurate total energies as well as
258 all the electronic and magnetic properties. Long-range dispersion interactions were
259 modeled using the D2 semi-empirical method of Grimme (Grimme, 2006). The
260 optimization of the structures was conducted *via* the conjugate-gradients method,
261 which stopped when the forces on all atoms were smaller than $0.01 \text{ eV}\cdot\text{\AA}^{-1}$. The
262 Dudarev *et al.* (Dudarev et al., 1998) approach was used within the DFT+*U*
263 methodology (Anisimov et al., 1992) to improve the description of the localized and
264 strongly correlated Fe *d* states, which were corrected by applying the value of $U_{\text{eff}} =$
265 3.7 eV (Santos-Carballal et al., 2018; Santos-Carballal et al., 2014). All calculations
266 were spin-polarised and the initial magnetic moments were set following a high-spin
267 ferrimagnetic structure, *i.e.* with opposite spins in the tetrahedral and octahedral sites
268 (Neel, 1948; Shull et al., 1951). These criteria allowed convergence of the total
269 electronic energy within 10^{-4} eV per atom. We decided to only model the magnetite
270 (001) surface as this is the thermodynamically most stable facet, with the lowest
271 relaxed surface energy and the most prominent plane in the calculated crystal
272 morphology (Santos-Carballal et al., 2014), which is in agreement with the
273 observations made by Zhao *et al.* at $\text{pH} \leq 13$ (Zhao et al., 2008). Moreover, Jönsson
274 and Sherman found that the bidentate interaction of the inner-sphere As(V) complexes
275 is only possible at the rows of exposed Fe_B ions formed in the [011] direction of the
276 magnetite (001) surface (Jonsson and Sherman, 2008), which is in line with its largest

277 density of exposed Fe cations (Santos-Carballal et al., 2014). However, similar to
278 goethite, we cannot rule out that that arsenate and phosphate may have different
279 affinities for other less stable and less prominent magnetite surfaces, which may
280 saturate with a small fraction of the total number of adsorbed oxyanions (Kubicki et
281 al., 2012), thus providing a minor contribution to the observed infrared spectra. For
282 the inner-sphere complexes, the adsorption of the phosphate and arsenate species on
283 the $\text{Fe}_3\text{O}_4(001)$ surface was simulated under both acid and alkaline conditions.
284 Different initial binding geometries, including MM, BM, BB and tridentate trinuclear
285 (TT), were taken into account. All possible binding sites were also inspected,
286 including the protruding Fe_A atom and the Fe_B ion as well as their possible
287 combinations. Thus, we are confident that we have considered all possible adsorption
288 geometries for the oxyanion complexes. However, given the large positional degree of
289 freedom of the water molecules, there may be some uncertainty in their location, but
290 this lies beyond the scope of this work. Further details of the computational methods
291 used, including surface models, inner- and outer-sphere complex models, approach
292 used for the simulation of acid and alkaline conditions, calculation of adsorption
293 energy, Bader charges and vibrational frequencies are presented in Text A.3 and
294 Figure A.2.
295

RESULTS AND DISCUSSION

296

297 **Individual molecular adsorption**

298 Arsenate adsorption on magnetite

299 The intensity of characteristic bands obtained by *in situ* ATR-FTIR was
300 proportional to the level of adsorption; as pH decreased, the arsenate adsorption was
301 obviously enhanced (Figure A.3). Given the point of zero charge (PZC) of magnetite
302 at 6.8 (Table A.1), the surface of this mineral gradually changed from negative charge
303 at alkaline pH to positive charge under acid conditions, improving the adsorption of
304 arsenate oxyanions. Besides band intensity, the spectrum profile also showed
305 significant changes with pH. At high pH, the spectra displayed a broad but
306 asymmetrical band at 855 cm^{-1} , with a shoulder peak at 820 cm^{-1} . As the pH decreases,
307 the band at 855 cm^{-1} became more symmetrical and sharpened, which was also
308 characteristic of aqueous HAsO_4^{2-} (Figure. A.4). Thus, outer-sphere (OS) HAsO_4^{2-}
309 complexes were formed on magnetite at acidic pH, which was verified in desorption
310 experiments at $\text{pH} = 4.0$ (Figure. A.5). Once the arsenate solution was replaced by
311 NaCl solution, the intensity of the band at 855 cm^{-1} quickly decreased in 10 min, and
312 then slowly declined in the following 140 min, suggesting the coexistence of both OS
313 and inner-sphere (IS) arsenate complexes, as OS species have faster desorption rates
314 than IS species (Catalano et al., 2008). According to previous work, neither As(III)
315 oxidation nor As(V) reduction occurs on the magnetite surface (Jonsson and Sherman,
316 2008).

317 According to the 2D-COS analysis results (Text A.5), the band at 855 cm^{-1} and those

318 at 870, 830 and 805 cm^{-1} are attributed to different adsorption complexes of arsenate.
319 The band at 855 cm^{-1} was identical to that of aqueous HAsO_4^{2-} (Figure A.4),
320 supporting the formation of these OS complexes. The contribution at 870 cm^{-1} was
321 assigned to the asymmetric stretching (ν_3) of As-O, while those at 830 and 805 cm^{-1}
322 were assigned to the asymmetric and symmetric stretchings (ν_3) of As-OFe,
323 respectively (Brechbuhl et al., 2012; Hu et al., 2015). The presence of three ν_3 bands
324 indicated the C_{2v} or lower symmetry for the IS arsenate complexes. The above
325 characteristic bands are consistent with the observations of arsenate adsorption on
326 ferrihydrite, hematite and rutile (Brechbuhl et al., 2012; Hu et al., 2015). Gao et al.
327 attributed the IR bands at 830 and 804 cm^{-1} to the arsenate adsorbed in the BB
328 geometry on the ferrihydrite surfaces at high pH (Gao et al., 2013). The BB
329 complexes are also the dominant geometry of arsenate adsorbed on most iron
330 (hydr)oxides, as verified by EXAFS (Jonsson and Sherman, 2008; Sherman and
331 Randall, 2003). Thus, in this study, the IS arsenate complexes on magnetite were also
332 assigned to the BB geometry.

333 The ATR-FTIR spectra were deconvoluted to gain additional insight into the arsenate
334 adsorption geometries (Figure. 1a). The relative amounts of adsorbed OS and IS
335 species and their contributions to the total adsorption (based on the sub-spectral area)
336 varied with pH (Figure. 2a). At $\text{pH} > 7$, almost no OS complexes were formed,
337 ascribed to the electrostatic repulsive force between the arsenate oxyanions and the
338 negatively charged magnetite surface. The IS complexes with BB geometry are the
339 main species at high pH (Eq. (1)). As the pH decreased, the magnetite surface became

340 positively charged, leading to the rapid increase in both the adsorption and
341 contribution of OS complexes (Eq. (2)). Once the OS complexes were formed, the
342 Coulombic attraction between the magnetite surface and arsenate oxyanions further
343 improved the formation of IS complexes with BB geometry by ligand exchange.
344 These findings explain why the IS species dominate over the OS complexes
345 throughout the studied pH range.



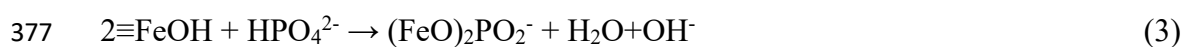
348

349 Phosphate adsorption on magnetite

350 The adsorption of phosphate on magnetite was also affected by pH (Figure. A.7).
351 When pH decreased from 9.0 to 4.0, the IR spectra increased in intensity, and
352 displayed variations in shape. Specifically, a blue-shift of the highest peak from 1028
353 ($\text{pH} = 9.0$) to 1050 cm^{-1} ($\text{pH} = 4.0$) was seen, alongside the appearance of two
354 shoulder peaks at 1000 and 1100 cm^{-1} . The IR spectra of the adsorbed phosphate were
355 clearly different from the aqueous phosphate oxyanions at identical pH (Figure. A.8),
356 suggesting the formation of IS complexes. This is also confirmed in the desorption
357 experiment at $\text{pH} = 4.0$ (Figure. A.9), where the IR intensity only decreased slightly
358 after desorption for 180 min.

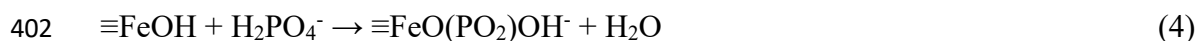
359 Based on the 2D-COS analysis (Text A.5), the IR bands of phosphate at 1075, 1028
360 and 965 cm^{-1} and those at 1108, 1050, 1000 and 870 cm^{-1} were assigned to different
361 IS complexes of phosphate. Both complexes had three ν_3 vibrations, indicating a C_{2v}

362 symmetry or lower. Through the deconvolution of the spectra (Figure. 1b) and the
363 calculation of its sub-spectral area (Figure. 2b), the contribution of each predominant
364 adsorbed phosphate complex was calculated at acid and alkaline pH (Figure. 2b).
365 Based on the very close IR signals at high pH, a complex with similar coordination
366 environment and protonation degree to 1075, 1028 and 965 cm^{-1} was reported for the
367 adsorption of phosphate onto ferrihydrite (1070, 1025 and 940 cm^{-1}) (Arai and Sparks,
368 2001; Carabante et al., 2010). These complexes were in a non-protonated form, as
369 confirmed through the comparison of spectra obtained in D_2O and H_2O medium (Arai
370 and Sparks, 2001). Considering their C_{2v} or C_1 symmetry and the alkaline pH range of
371 stability, these non-protonated species were affiliated to BB complexes (Eq. (3)) (Arai
372 and Sparks, 2001; Kubicki et al., 2012), which were also reported in the adsorption of
373 phosphate on goethite (1089, 1044 and 945 cm^{-1}) (Kubicki et al., 2012) and hematite
374 (1085, 1035, and 966 cm^{-1}) (Elzinga and Sparks, 2007). The bands at 1075 and 1028
375 cm^{-1} were attributed to the stretching of the PO_2 bond, while the 965 cm^{-1} peak
376 belonged to Fe-O-P bending.



378 The dominant complexes at acid pH were the protonated species. In previous studies,
379 the characterization of their coordination environments and protonation degree were
380 controversial (Arai and Sparks, 2001; Elzinga and Sparks, 2007; Luengo et al., 2006;
381 Tejedortejedor and Anderson, 1990), as the formations of $(\text{XO}_3)\text{PO}$ and $(\text{XO}_2)\text{PO}_2$
382 ($\text{X}=\text{Fe}$ or H) were suggested. Protonated $(\text{XO}_3)\text{PO}$ species, including monoprotinated
383 BB complexes ($(\equiv\text{FeO})_2(\text{OH})\text{PO}$, MBB) and di-protonated MM complexes

384 ($\equiv\text{FeO}(\text{OH})_2\text{PO}$, DMM), were reported for the adsorption on ferrihydrite (1124, 1035
385 and 998 cm^{-1}) (Carabante et al., 2010), goethite (1123, 1006 and 982 cm^{-1}) (Luengo et
386 al., 2006; Tejedortejedor and Anderson, 1990), and hematite (1120, 1010 and 970 cm^{-1})
387 (Elzinga and Sparks, 2007). The bands at high frequency ($\geq 1120\text{ cm}^{-1}$) were
388 attributed to the P=O stretching of the $(\text{XO}_3)\text{PO}$ species (Arai and Sparks, 2001;
389 Elzinga and Sparks, 2007). The adsorption geometry of protonated $(\text{XO}_2)\text{PO}_2$, i.e.,
390 monoprotonated MM ($\equiv(\text{FeO})(\text{OH})\text{PO}_2$), was identified on ferrihydrite (1100, 1028
391 and 920 cm^{-1}) (Arai and Sparks, 2001) and hematite (1115, 1006 and 970 cm^{-1})
392 (Elzinga and Sparks, 2007). For these complexes, bands at ~ 1100 and $\sim 1115\text{ cm}^{-1}$
393 were assigned to the PO_2 group since its frequencies were between $\nu_{\text{P=O}}$ (1120 cm^{-1})
394 and $\nu_{\text{P-Ofc}}$ (1000 cm^{-1}) (Tejedortejedor and Anderson, 1990). In the present study, the
395 phosphate complexes (1108, 1050 and 1000 cm^{-1}) that predominated at acid pH were
396 monoprotonated MM complexes (MMM) (Eq. (4)), as the band with the highest
397 frequency (1108 cm^{-1}) was too low to be assigned to the P=O stretching. The bands at
398 1108 and 1050 cm^{-1} were attributed to the stretching of the PO_2 bond, while those at
399 1000 and 870 cm^{-1} belonged to the Fe-O-P and P-OH bending, respectively. The
400 formation of the FeOPO_3 (C_{3v}) complexes were excluded, as they have a molecular
401 symmetry higher than the lowest C_{2v} allowed.



403

404 **Competitive molecular adsorption**

405 Substitution of phosphate by arsenate

406 At pH = 4, the MMM complexes are the dominant phosphate species followed by the
407 NBB complexes (Figure. 2b). When the phosphate solution was substituted by an
408 arsenate solution of equal molar concentration, the bands of phosphate (1200–870
409 cm^{-1}) immediately decreased in intensity, suggesting their desorption from the
410 magnetite surface (upper panel of Figure. 3a). Simultaneously, the bands assigned to
411 the adsorbed arsenate in the region of 900–800 cm^{-1} appeared and their intensity
412 increased with the adsorption time. This became more obvious upon subtracting the
413 equilibrium spectrum for the adsorbed arsenate recorded at 270 min, from the signals
414 recorded at 135 min, i.e., immediately before the introduction of arsenate. This
415 subtraction highlighted only the bands for which intensity decreased (positive bands)
416 or increased (negative bands) (lower panel of Figure. 3a). Based on the spectral
417 integration, 32% of adsorbed phosphate was replaced by arsenate. The proportion of
418 phosphate substituted by arsenate was close to the replacement found in previous
419 studies using ferrihydrite and goethite (O'Reilly et al., 2001). For example, Carabante
420 et al. reported that 35% of phosphate was desorbed from the ferrihydrite surface by
421 arsenate using D_2O as solvent at $\text{pD} = 4$ (Carabante et al., 2010), while Liu et al. and
422 Neupane et al. found that between 26%-28% of the adsorbed phosphate on goethite
423 and ferrihydrite surfaces was replaced by arsenate (Liu et al., 2001; Neupane et al.,
424 2014). In order to determine the coordination environments, the positive bands in the
425 range 1200-870 cm^{-1} were deconvoluted into three contributions at 1108, 1050 and

426 1000 cm^{-1} , which were assigned to MMM phosphate complexes. Moreover, the
427 negative bands at 870, 827 and 801 cm^{-1} were attributed to arsenate BB complexes
428 (Figure. 3a).

429 Similar competitive experiments were also conducted under neutral ($\text{pH} = 7$, Figure.
430 3b) and alkaline conditions ($\text{pH} = 9$, Figure. 3c), where partial substitution of
431 phosphate by arsenate was also observed. At $\text{pH} = 7.0$, the amount of phosphate
432 adsorbed as MMM and NBB complexes were comparable (Figure. 2b). However, the
433 integral spectrum of the NBB complexes (1075, 1026 and 960 cm^{-1}) was much lower
434 than for the MMM complexes (1100, 1050, 1000 cm^{-1} , Figure. 3b). The differences
435 between the integrals of these bands indicates that the desorption of the MMM
436 complexes was more significant than for the NBB, which was also found in the
437 desorption of phosphate from ferrihydrite (Carabante et al., 2010).

438 To enhance the IR signal of the IS species at alkaline pH (Figure. 2), the
439 concentrations of both phosphate and arsenate were increased from 100 $\mu\text{mol L}^{-1}$ to
440 500 $\mu\text{mol L}^{-1}$ (Figure. 3c). The desorption of phosphate ($\sim 15\%$) was lower under
441 alkaline conditions than at acid pH ($\sim 32\%$) (Figure. 3a), where the removal of both
442 MMM and NBB complexes was comparable. Based on the integral area of the
443 difference spectrum, the proportion of desorbed NBB complexes was below 15% of
444 the total adsorbed phosphate. Moreover, the NBB complexes required 350 min to
445 achieve desorption equilibrium, which was much slower than the removal of MMM at
446 acid and neutral pH (135 min).

447

448 Substitution of arsenate by phosphate

449 At pH = 4, the adsorbed arsenate was mainly forming BB complexes, with a low
450 proportion of OS species (Figure. 2a). After the introduction of phosphate solution of
451 equal molar concentration, the bands in the region of 1200–900 cm⁻¹ corresponding to
452 phosphate appeared immediately and increased in intensity with time (Figure. 4a),
453 illustrating adsorption on magnetite surfaces. However, the IR intensity of arsenate
454 initially decreased slightly (~10%), but then stabilized, which suggests that the
455 phosphate oxyanions can only substitute partially the pre-adsorbed arsenate. After
456 subtracting the spectrum recorded just before the addition of phosphate and after its
457 adsorption had reached equilibrium, at 135 min and 270 min, respectively, the
458 positive bands related to adsorbed phosphate were located at 1108, 1050 and 1000
459 cm⁻¹. As mentioned above, these bands were associated with the MMM phosphate
460 complexes prevalent at acid pH. The negative bands that appeared at 852 and 798
461 cm⁻¹ were attributed to the As-O asymmetrical stretching (ν_3) and the As-OH vibration
462 of the arsenate OS species (Hu et al., 2015).

463 Similarly to the competitive adsorption at pH = 4, phosphate could not substitute the
464 pre-adsorbed arsenate at neutral pH (Figure. 4b). The introduction of phosphate did
465 not lead to a decrease in the IR intensity of arsenate. Although the individually
466 adsorbed phosphate species in neutral conditions were in equal proportions in both
467 MMM and NBB geometries (Figure. 2b), only the former configuration was stable
468 upon introduction of arsenate, as indicated by the phosphate bands at 1106, 1049, 994
469 and 896 cm⁻¹. Meanwhile, the difference spectrum did not show evidence of signals

470 from the desorbed arsenate, which confirms that the arsenate BB complexes are the
471 dominant adsorption configuration, with a higher binding affinity than both the MMM
472 and NBB phosphate complexes.

473 At alkaline pH, the amount of arsenate that adsorbed onto magnetite was low,
474 resulting in a poor signal-to-noise ratio for the spectra. Thus, competitive adsorption
475 under alkaline conditions was not analyzed in this study.

476

477 **DFT calculations**

478 Outer-sphere complexes

479 The outer-sphere (OS) complexes comprising the solute surrounded by water
480 molecules are displayed in Figure. A.11. P-based anions are consistently smaller than
481 their As-containing counterparts, as the intramolecular mean distance from the central
482 atom to the oxygen ions differs by ~ 0.17 Å (Table 1). The degree of protonation of the
483 solute does not noticeably affect the single and double bond distances (Table 1). As
484 expected, the Bader charges of the solute ions are underestimated by $\sim 17\%$ with
485 respect to their formal charges, which increases to $\sim 23\%$ with the pH value (Table 2).
486 For the outer-sphere complexes under alkaline conditions, a charge of approximately
487 $-0.66 e^-$ was calculated for the OH groups (Table 2), which prefer to coordinate the
488 protruding Fe_A ion at 1.92 and 1.95 Å for $HAsO_4^{2-}$ and HPO_4^{2-} , respectively (Figure.
489 A.11).

490 Figure A.11 displays the radial distribution functions for $H_2PO_4^-$, HPO_4^{2-} , $H_2AsO_4^-$,
491 and $HAsO_4^{2-}$, where the radii are measured from the central atom of the P or As solute

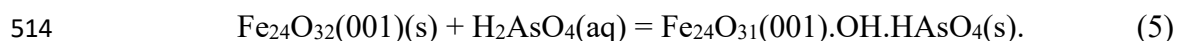
492 to the O of the water molecules. The main hydration shells for these oxyanions lie
493 between 3.5 and 6.0 Å, which is in excellent agreement with the molecular dynamics
494 (MD) simulations of Pathak and Bandyopadhyay (2016) for AsO_4^{3-} and supports the
495 suitability of the size of our water simulation box (Pathak and Bandyopadhyay, 2016).
496 Under acid conditions, the di-protonated arsenate (H_2AsO_4^-) and phosphate (H_2PO_4^-)
497 ions are the dominant species with C_{2v} symmetry and 15 fundamental vibrational
498 modes. Alkaline pH values lead to the deprotonation of the outer-sphere complexes,
499 thus increasing their symmetry to the C_{3v} molecular point group, with a reduction to 3
500 singly degenerate vibrations for the H atom. Generally, most of the fundamental
501 vibrational modes for As-containing anions are red-shifted with respect to their
502 phosphate counterparts, in excellent agreement with the ATR-FTIR experiments
503 (Table 3). The only exceptions are the stretching $\nu(\text{PO-H})$ and bending $\delta(\text{POH})$ mode
504 for HPO_4^{2-} and H_2PO_4^- , respectively, which appear at higher wavenumbers than for
505 the iso-structural As-based molecules. However, taking into account that the bending
506 $\delta(\text{POH})$ is 1245 cm^{-1} for H_2PO_4^- at acid pH (Table 3), which compares closely with
507 the experimental value of 1240 cm^{-1} (Figure. A.8), we are confident of the predictive
508 accuracy and consistency of our approximate vibrational modes. More details about
509 the DFT results of outer-sphere complexes are described in Text. A.4.

510

511 Arsenate adsorption on the $\text{Fe}_3\text{O}_4(001)$ surface

512 The dissociative adsorption process of the H_2AsO_4^- solute onto the $\text{Fe}_3\text{O}_4(001)$

513 surface at acid pH can be represented as Eq. (5):

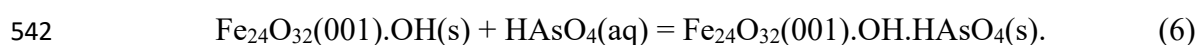


515 HAsO_4^{2-} in the BB configuration is the most thermodynamically stable inner-sphere
516 complex calculated for arsenate (Figure. 5a), with the largest adsorption energy of
517 -2.19 eV per molecule (Table 2). The surface Fe_B ions coordinate the adsorbate O
518 atoms at 2.06 Å, which reduces their electronic density and induces an elongation of
519 the As=O bond distances by 0.03 Å with respect to the outer-sphere complexes. The
520 O–As=O and particularly the O=As=O bond angles become narrower after adsorption,
521 but the latter still remains wider than the former (Table 1). The dissociated proton
522 binds a neighboring surface O atom at 1.02 Å, which is a slightly larger bond distance
523 than in any of the other discussed solutes. The computed As-O bond length and As-Fe
524 distance of the BB arsenate complex are ca. 1.71 and 3.20 Å, respectively, which is
525 consistent with the values (1.69 and 3.42 Å) obtained from EXAFS analysis (Jonsson
526 and Sherman, 2008).

527 The acid proton has a typical charge of 0.67 e^- , while the inner-sphere complexes gain
528 0.60 e^- compared to the di-protonated molecule in solution. Consistent with the
529 presence of two types of H atoms, *i.e.*, in the inner-sphere complexes and directly
530 attached to the surface, six singly degenerate vibrational modes associated with these
531 atoms are found (Table 3). The stretching $\nu(\text{AsO-H})$ and bending $\delta(\text{AsOH})$ in the
532 adsorbed molecule are red-shifted with regard to the outer-sphere complexes, in line
533 with their different chemical environments. The stretching modes involving the
534 central As atom have the typical pattern of BB complexes. For instance, the largest
535 wavenumber of 816 cm^{-1} is assigned to the As=O bond, whereas the intermediate

536 vibrations between 751 and 786 cm^{-1} are calculated for the symmetric and asymmetric
537 $\nu(\text{As}-\text{OFe})$. In agreement with its largest distance, the softer mode is computed for
538 the single bond between the central atom and the protonated oxygen.

539 Unlike the outer-sphere H_2AsO_4^- complexes, which adsorb dissociatively in acid
540 environment, the HAsO_4^{2-} anion does not change its stoichiometry after binding to the
541 $\text{Fe}_3\text{O}_4(001)$ surface at alkaline pH (Eq. (6)):



543 The mono-protonated adsorbed As-containing molecule interacts with two Fe_B surface
544 ions, forming a bidentate (BB) configuration that resembles the inner-sphere
545 complexes of arsenate at acid pH (Figure. 5b).

546 However, the presence of an adsorbed OH^- group rather than H^+ causes noticeable
547 energetic and structural changes in the adsorbate. The adsorption energy increases by
548 1.35 eV per HAsO_4^{2-} molecule when the pH changes from acid to alkaline, becoming
549 comparable to the experimental value reported by Sabur and coworkers for arsenate at
550 neutral pH conditions (Sabur et al., 2015). The $\text{Fe}_B\text{-O}$ bonds between the molecule
551 and surface are 0.07 Å shorter at high than at low pH. The bond distance from the
552 central As atom to the hydroxy group is stretched from 1.76 to 1.86 Å following the
553 increase in pH. After adsorption, the adsorbed OH group moves 0.08 Å away from the
554 surface and leans towards a nearby surface O atom to form a hydrogen bond. Table 1
555 shows that the relative order $\angle(\text{O}-\text{As}=\text{O}) < \angle(\text{O}=\text{As}=\text{O})$ is restored for the bond
556 angles upon the formation of the inner-sphere complexes. Despite the same
557 stoichiometry, the Bader charge analysis reveals that the adsorbate loses 0.14 e^- after

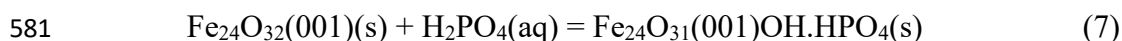
558 adsorption, but the charge of the OH^- remains almost unaffected at $-0.68 e^-$.
559 Owing to the similar adsorption configuration for HAsO_4^{2-} at both acid and alkaline
560 pH, the number and type of fundamental vibrational modes in these two conditions
561 are the same. However, all vibrations shift for HAsO_4^{2-} as a result of the change in pH
562 (Table 3). For example, the wavenumber for $\nu(\text{As-OH})$ increases greatly to 3007 cm^{-1} ,
563 whereas $\omega(\text{AsOH})$ is red-shifted to 830 cm^{-1} . The increase in pH has a strong impact
564 on the stretching mode of the elongated As-OH bond of the surface-immobilized
565 HAsO_4^{2-} species. Moreover, the formation of the inner-sphere arsenate complexes and
566 $\text{FeOH}\cdots\text{H}$ hydrogen bond have a major effect on the $\nu(\text{FeO-H})$ and $\omega(\text{FeOH})$ modes.
567 Our DFT predicted vibrational frequencies for the hardest modes $\nu(\text{As=O})$ and
568 $\nu(\text{As=OFe})$ of the inner-sphere HAsO_4^{2-} complex under both acid and alkaline
569 conditions are under-estimated by $\sim 60 \text{ cm}^{-1}$ with respect to the experimental values.
570 However, the deviation between the ATR-FTIR spectra and the simulated frequency is
571 90 and 190 cm^{-1} under acid and alkaline conditions, respectively, for the softer mode
572 $\nu(\text{As-OH})$.

573

574 Phosphate adsorption on the $\text{Fe}_3\text{O}_4(001)$ surface

575 Among the various possible binding geometries of phosphate onto magnetite, the
576 mono-protonated monodentate mononuclear (MMM) mode is the most stable
577 adsorption configuration at acid pH, wherein the HPO_4^{2-} anion binds the Fe_B surface
578 cation and releases 1.89 eV per molecule (Table 2 and Figure. 6a). The dissociative
579 adsorption of H_2PO_4^- on the $\text{Fe}_3\text{O}_4(001)$ surface at acid conditions can be represented

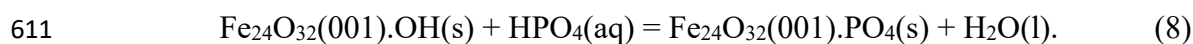
580 by Eq. (7):



582 As shown in Figure. 6a, the dissociated proton prefers to interact at 0.98 Å with a
583 nearby surface oxygen atom to form acid $\text{Fe}_{24}\text{O}_{31}(001).\text{OH}$ groups rather than H_3O^+
584 cations in solution. The strong chemisorption is characterized by the
585 adsorbate-surface $\text{PO}-\text{Fe}_B$ interatomic bond distance of 2.08 Å, which is only 0.02 Å
586 larger than the $\text{O}-\text{Fe}_B$ distance in the bulk of Fe_3O_4 (Table 1). The average $\text{P}=\text{O}$
587 distances for the outer- and inner-sphere P-containing complexes are very close at
588 acid pH. Compared to H_2PO_4^- in solution, the $\text{P}-\text{O}$ bond stretches, whereas the $\text{PO}-\text{H}$
589 bond distance decreases by approximately 0.05 Å for the adsorbed HPO_4^{2-} . The
590 $\text{O}-\text{P}=\text{O}$ bond angle experiences the largest change, from 109.06° to 105.01° , given
591 that the adsorbate loses half of its single bonded O atoms during the dissociative
592 adsorption of H_2PO_4^- . The charge of the dissociated H is $0.65 e^-$, while the adsorbed
593 anion becomes $0.66 e^-$ more negative than its parent ion in solution (Table 2).
594 Dissociative adsorption of H_2PO_4^- in the MMM configuration causes its molecular
595 point group to reduce to C_s and to 12 the total number of fundamental vibrational
596 modes. After binding to the surface, the POH wagging is not detected above 600 cm^{-1} ,
597 while the $\text{PO}-\text{H}$ stretching is shifted to 3625 cm^{-1} and the POH bending is red-shifted
598 by approximately 200 cm^{-1} (Table 3). In line with the new symmetry, the two largest
599 stretching modes are assigned to $\text{P}=\text{O}_2$, whereas 942 cm^{-1} corresponds to $\text{P}-\text{OFe}$ and
600 the lowest wavenumber is calculated for the protonated O atom. For the dissociated
601 proton, the $\text{FeO}-\text{H}$ stretching as well as the FeOH bending and wagging were

602 obtained at the usual position for OH groups. The calculated vibrational frequencies
603 were also underestimated for the inner-sphere phosphate complexes in acid conditions,
604 with the largest discrepancy observed for the modes with the smallest wavenumber.
605 For example, the simulated values for the hardest $\nu(\text{P}=\text{O})$ modes were just 5 and
606 20cm^{-1} below the experimental frequencies; while the difference for the softer (softest)
607 $\nu(\text{P}=\text{OFe})$ [$\nu(\text{P}-\text{OH})$] mode was 60 (104) cm^{-1} .

608 Under alkaline conditions, HPO_4^{2-} prefers to adsorb dissociatively onto the $\text{Fe}_3\text{O}_4(001)$
609 surface, forming the non-protonated bidentate binuclear (NBB) inner-sphere complex
610 and liquid water as follows:



612 This process releases 0.69 eV per molecule, which is the weakest adsorption energy
613 reported in this study (Table 2). Two O atoms from the anion coordinate the surface
614 Fe_A and Fe_B ions at 1.91 and 1.95 Å, respectively (Table 1 and Figure. 6b). A small
615 stretch in the P=O bond from the average value of 1.56 Å is also observed in those
616 atoms directly interacting with the surface, whereas the bond angles remain perfectly
617 tetrahedral at 109.44° . The Bader charge for the inner-sphere PO_4^{3-} complex is -2.13
618 e^- , which is the largest reported in this paper. The charge of the fully deprotonated
619 phosphate ion explains its small adsorption energy, caused by the strong Coulombic
620 repulsion at the negatively charged $\text{Fe}_3\text{O}_4(001)$ surface. The PZC of magnetite at 6.8
621 suggests that at alkaline pH, the Fe_3O_4 surfaces become negative due to adsorbed OH^-
622 groups.

623 Despite its C_s point group, the adsorbed NBB PO_4^{3-} species has the simplest set of

624 vibrational frequencies with only 4 measurable fundamental modes (Table 3). The
625 largest frequencies are for the asymmetric and symmetric P=O modes, at 1111.64 and
626 948.85 cm^{-1} , respectively. The longest and weakest P–OFe bonds are characterized by
627 the smallest frequencies, which were calculated at 909 and 884 cm^{-1} for the
628 asymmetric and symmetric modes, respectively.

629 Although phosphate OS complexes are smaller than their arsenate counterparts (Table
630 1), the three solvation shells found are formed roughly at the same distance from the
631 central atom for the two different oxyanions, which essentially remain tetrahedral.
632 However, when the phosphate and arsenate molecules approach the $\text{Fe}_3\text{O}_4(001)$
633 surface, they form IS complexes of different geometries and number of interactions
634 with the exposed Fe ions. The adsorption energies show that under both acid and
635 alkaline conditions arsenate prefers to form MBB complexes with two neighboring
636 Fe_B ions from the $\text{Fe}_3\text{O}_4(001)$ surface. However, phosphate forms an NBB complex
637 with the exposed Fe_A and Fe_B ions at alkaline pH, while HPO_3^{2-} coordinates a single
638 Fe_B ion as an MMM species under acid conditions (Figures. 6 and 7). On
639 thermodynamic grounds, arsenate species bind more strongly to the $\text{Fe}_3\text{O}_4(001)$
640 surface than the phosphate complexes under acid and alkaline conditions (Table 2),
641 which explains the stronger adsorption affinity of arsenate over phosphate. The
642 oxyanions release the largest adsorption energies under acid conditions and the
643 calculated Bader charges explain the trends found for the adsorption energies.
644 Adsorption reduces the molecular point group of the oxyanions, which impacts the
645 frequency of the four stretching modes involving the central atom and the oxygen

646 atoms (Table 3). The shift of the vibrational modes for the adsorbed oxyanions with
647 respect to the OS complexes offers an unambiguous route to characterize the
648 geometry and coordination number of the IS species.

649

650 Effect of pH on individual and comparative adsorption

651 During individual molecular adsorption of equal amounts of arsenate and phosphate,
652 their adsorption edges have very similar curve profiles, in agreement with previous
653 works (Arai and Sparks, 2001; Jia et al., 2007; Luengo et al., 2006). In this study, the
654 arsenate and phosphate adsorption increased gradually on magnetite as the pH
655 decreased (Figures. A.3 and A.6), ascribed to the positive charge of the mineral
656 surface. Such variations have also been observed in the individual adsorption of
657 arsenate and phosphate onto goethite, which is the most studied mineral adsorbent
658 (Hingston et al., 1971; Liu et al., 2001; Manning and Goldberg, 1996). As reported by
659 Liu et al., the surface coverage of phosphate and arsenate on goethite was 112 and 109
660 mol kg⁻¹ at pH = 8, respectively, which values increased to 193 and 197 mol kg⁻¹ at
661 pH = 3. Although the individual arsenate and phosphate adsorption showed similar
662 dependence on the pH, the binding efficiency was greatly affected by pH during
663 competitive adsorption. In this study, when pre-adsorbed on magnetite, 32% of
664 phosphate was desorbed in the presence of arsenate at pH = 4 (Figure. 5), while only
665 15% was desorbed at pH = 9 (Figure. 7). The phosphate adsorption strength increased
666 with pH, which was also observed during adsorption onto goethite and ferrihydrite.
667 Liu et al. found that, in the presence of arsenate, the efficiency of phosphate

668 adsorption on goethite increased from 50% (pH = 3) to 70% (pH = 8) and was not
669 significantly influenced at alkaline pH, i.e., 69% (pH = 7), 70% (pH = 8) and 72%
670 (pH = 9) (Liu et al., 2001). In order to evaluate the ability of phosphate (or arsenate)
671 to depress the adsorption of arsenate (or phosphate) during competitive adsorption,
672 the competition efficiency (%) of phosphate η_P was calculated as $\eta_P = 100$
673 $\times(1-N_{\text{arsenate}}/N^0_{\text{arsenate}})$, where N_{arsenate} was the amount of arsenate adsorbed in the
674 presence of phosphate and N^0_{arsenate} was the amount of arsenate individually adsorbed
675 (Liu et al., 2001). The obtained results show that, independently of pH, the
676 competition efficiency of arsenate over phosphate ranged from 70 to 74%. In contrast,
677 phosphate was more stable under alkaline than acid conditions.

678 The pH effect on the competitive adsorption efficiency between phosphate and
679 arsenate has been observed in previous studies. For example, in soils, the inhibitory
680 effect of phosphate toward arsenate adsorption is stronger than the other way round
681 when the pH is higher than 6 (Melamed et al., 1995; Peryea, 1991). Gao and Mucci
682 reported that the phosphate introduction obviously restrained the arsenate adsorption
683 on goethite at alkaline pH. The arsenate addition, even in excess, led to only slight
684 decrease in the amount of phosphate adsorbed (Gao and Mucci, 2001). These findings
685 are different from ours, where the individual arsenate and phosphate adsorptions were
686 found to be comparable at alkaline pH. However, the affinity towards goethite is
687 stronger for arsenate than for phosphate at acid pH (Carabante et al., 2009; Violante
688 and Pigna, 2002; Zhao and Stanforth, 2001), which becomes comparable under
689 neutral conditions (Manning and Goldberg, 1996). Therefore, pH plays a vital role in

690 the competitive adsorption between arsenate and phosphate.

691

692 Effect of adsorption sequence on individual and comparative adsorption

693 The simultaneous or successive addition of oxyanions is important in the context of

694 competitive adsorption (Carabante et al., 2010; Liu et al., 2001). In nature,

695 environmental substances are more commonly adsorbed onto minerals sequentially

696 than simultaneously. When pre-adsorbed arsenate was replaced by phosphate on

697 goethite, the competition efficiency of arsenate and phosphate remained constant at

698 70–74% and 20%, respectively, independent of pH (Liu et al., 2001). However,

699 substitution of pre-adsorbed phosphate by arsenate led to an increase of the

700 competition efficiency of phosphate from 50% (acid pH) to 65% (alkaline pH), while

701 arsenate decreased from 30% (acid pH) to 10% (neutral pH). For the simultaneous

702 addition of the adsorbates, the efficiency of arsenate and phosphate was 50% and 40%,

703 respectively. Although the competitive adsorption experiment was carried out using

704 different adsorption sequences, arsenate was always adsorbed more strongly than

705 phosphate, indicating that arsenate has the highest affinity towards the goethite

706 surfaces. This was also found during the competitive arsenate and phosphate

707 adsorption onto magnetite and ferrihydrite (Carabante et al., 2010). For example, as

708 reported in this study, the amount of phosphate adsorbed decreased by 32% after the

709 introduction of arsenate at equal concentration under acid conditions. Conversely, the

710 subsequent addition of phosphate only resulted in about 10% arsenate desorption.

711 This is consistent with the results from the DFT calculations, where it was found that

712 arsenate has stronger adsorption affinity to magnetite than phosphate.

713

714 Effect of mineral species on individual and comparative adsorption

715 Diverse competitive adsorption trends appear for phosphate and arsenate during

716 interaction with different mineral phases in soils. In general, the competitive ability

717 towards iron (hydr)oxides is stronger for arsenate than for phosphate. As mentioned

718 above, during the adsorption on ferrihydrite and goethite, the restraining effect of

719 arsenate on phosphate is obviously the strongest. A similar phenomenon is also seen

720 in this study, where arsenate has higher affinity for and stability on magnetite than

721 phosphate. However, the opposite was found when aluminum (hydr)oxides were the

722 mineral phases. Manning et al. investigated competitive adsorption of arsenate and

723 phosphate on goethite and gibbsite (Manning and Goldberg, 1996). On both mineral

724 phases, phosphate induced the desorption of *ca.* 15mmol kg⁻¹ of arsenate. However,

725 the arsenate addition only decreased the phosphate adsorption by 8mmol kg⁻¹ on

726 gibbsite, which indicates a preference for phosphate rather than arsenate. ~~The~~

727 Arsenate and phosphate also display similar competitive adsorption on calcite ~~and~~

728 aluminum (hydr)oxides. The arsenate adsorption is significantly inhibited by

729 phosphate, while the phosphate adsorption is barely affected by arsenate (So et al.,

730 2012).

731 In addition to the chemical formula of the mineral phases, the competitive adsorption

732 properties of arsenate and phosphate are also affected by the crystallinity of the

733 material. Xu et al. studied the effect of arsenate addition on the phosphate desorption

734 kinetics from crystalline and amorphous hydrargillite (Xu et al., 2008). Phosphate was
735 easily replaced by arsenate, which had the largest affinity for amorphous rather than
736 for crystalline hydrargillite, because of difference in the density of surface active sites.
737
738 Competitive adsorption mechanism
739 Despite the similar individual adsorption behavior, the mechanism for the competitive
740 adsorption between arsenate and phosphate onto the iron (hydr)oxide surfaces is still a
741 topic of debate. Phosphate with its smaller thermochemical radius is expected to have
742 the strongest affinity for these mineral phases, yet arsenate displays the strongest
743 preference, especially at acid pH.
744 During arsenate and phosphate adsorption onto iron (hydr)oxides, these oxyanions
745 adopt diverse geometries with different binding strengths. For example, phosphate
746 adsorbed on ferrihydrite displays two adsorption geometries, i.e., protonated BB and
747 non-protonated BB, as observed by *in situ* ATR-FTIR (Carabante et al., 2010).
748 Arsenate is mainly adsorbed in the BM and BB geometries, as determined by *in situ*
749 ATR-FTIR and XAFS (Carabante et al., 2010; Neupane et al., 2014). However, these
750 adsorption complexes display different affinities towards mineral surfaces. For
751 example, phosphate induces the desorption of the BM arsenate complexes, while the
752 BB arsenate complexes are less affected (Neupane et al., 2014), which indicates that
753 the stability is higher for the BB than for the BM arsenate species.
754 In this study, *in situ* ATR-FTIR and DFT calculations have revealed that phosphate
755 was individually adsorbed onto magnetite in the NBB and MMM geometries, while

756 arsenate mainly formed BB complexes with few OS species. However, under
757 competitive adsorption conditions, the BB arsenate complexes obviously substituted
758 both the MMM and to a lesser extent the NBB phosphate complexes. These findings
759 illustrate that NBB phosphate complexes are more stable than MMM complexes, and
760 also that their binding strength is weaker than for the BB arsenate complexes. The
761 competitive adsorption of phosphate and arsenate can be explained by variations in
762 adsorption geometries with pH. Under acid conditions, the dominant MMM
763 phosphate species had the smallest adsorption energies ($E_{\text{ads}} = -0.69$ eV, Table 2) and
764 were easily replaced by arsenate ($E_{\text{ads}} = -0.84$ eV). As pH increased, NBB became the
765 main phosphate species, displaying enhanced stability ($E_{\text{ads}} = -1.89$ eV), which
766 resulted in decreasing desorption by arsenate. Throughout the studied pH range, the
767 adsorbed arsenate remained in the BB geometry with higher stability than phosphate.
768 Thus, the competitive efficiency for phosphate increased with pH, while for arsenate
769 it remained almost stable. These results for magnetite are in excellent agreement with
770 the findings on goethite (Liu et al., 2001).

771 Besides the adsorption geometry, the Coulombic interaction between the positively
772 charged magnetite surfaces and negatively charged adsorbates is another important
773 factor controlling the competitive adsorption between arsenate and phosphate. Given
774 the magnetite PZC at 6.8, the electrostatic attraction with phosphate and arsenate
775 oxyanions increases as pH decreases. This improves the adsorption onto the magnetite
776 surface and thus, decreases the proportion of hydroxyl groups covering adsorption
777 sites. The adsorption geometry of phosphate species changes from NBB to MMM

778 complexes, which contain fewer protons. A similar variation in adsorption
779 complexation from binuclear to mononuclear is also observed during the adsorption
780 of arsenate onto ferrihydrite (Neupane et al., 2014). To form BB complexes with
781 higher stability than MM configurations, the oxyanions should be bound to two
782 adjacent protonated oxygen sites. However, only mononuclear complexes are formed
783 if the protonated oxygen site is far away from the adsorbate. Based on the shorter
784 intramolecular O...O distance in phosphate compared to arsenate (2.45 and 2.6–2.8 Å,
785 respectively), the latter is more likely to form BB complexes than the former (So et al.,
786 2012). Lumsdon et al. found that the interaction with hydroxyl sites was stronger for
787 arsenate than for phosphate, because of the different molecular sizes of the adsorbates
788 (Lumsdon et al., 1984). Thus, arsenate bidentate binuclear complexes dominate in
789 areas of high surface coverage, whereas monodentate species are only found in areas
790 of low surface coverage (Fendorf et al., 1997). In contrast, the large surface coverage
791 of phosphate species prefers the formation of monodentate complexes (Liu et al.,
792 2001), which was also found under the acidic condition in this study.

793 Compared to other iron oxides, the formation of abundant monodentate mononuclear
794 phosphate complexes on magnetite alongside a low proportion of arsenate OS species
795 is unique for this combination of substrate and adsorbates. The PZC value for
796 magnetite (~6.8) is lower than for goethite (~9.1), ferrihydrite (~7.6-8.1) or hematite
797 (~11), which leads to Fe₃O₄ displaying a lower degree of protonation than other iron
798 oxides at the same pH. Protonated surface sites facilitate IS surface complexation
799 because water is more easily displaced than hydroxyl groups (Johnston and

800 Chrysochoou, 2012). Thus, the decrease of protonation on the magnetite surface
801 results in the formation of more MM complexes of phosphate with fewer hydroxyl
802 groups, as well as OS species of arsenate. Similar variations have appeared in sulfate
803 adsorption, where IS complexes are exclusively found on hematite with the highest
804 PZC (Hug, 1997), and both OS and IS complexes are formed on ferrihydrite
805 (Johnston and Chrysochoou, 2014).

806

807

IMPLICATIONS

808 This study provides a molecular-level insight into the competitive adsorption between
809 arsenate and phosphate on magnetite surfaces. Magnetite has a widespread occurrence
810 in surface environment and is found coating the zero-valent iron nanoparticles
811 increasingly used for environmental engineering, especially for As removal. Thus, our
812 new results would be beneficial for assessing the environmental fate of arsenate and
813 phosphate, as well as for other ions that may compete for or otherwise react with the
814 magnetite surface sites.

815 Owing to the low surface site density of magnetite, its adsorption towards oxyanions
816 has seldom been surveyed by *in situ* techniques. In this study, with the aid of 2D-COS
817 analysis, we have resolved better the peaks of *in situ* ATR-FTIR spectra, which
818 greatly facilitates the identification of adsorption species and geometries of both
819 oxyanions. For phosphate, MMM complexes dominated at acid pH, while NBB
820 complexes were dominant at alkaline conditions. Arsenate mainly formed BB
821 complexes with some outer-sphere species, both of which were more prevalent at acid

822 than at alkaline pH. This is somewhat different from the cases on other iron oxides,
823 e.g., ferrihydrite and goethite, ascribed to the lower surface site density of magnetite.
824 The competitive adsorption of these adsorption species was further investigated by
825 ATR-FTIR for different substitution sequences, providing spectroscopic evidence for
826 their adsorption affinity towards magnetite surface. The adsorption strength was also
827 thermodynamically confirmed for the first time through DFT calculations. Therefore,
828 this study offers an important step forward in understanding the adsorption of
829 oxyanions in complex systems, which is more environmentally realistic.

830 The adsorption affinity of the geometries as observed increased in the following order:
831 MMM phosphate complex < NBB phosphate complex < BB arsenate complex. The
832 high stability of adsorbed arsenate suggests the vital role of magnetite in the transfer
833 and transformation of arsenic in surface environment. Meanwhile, magnetite could be
834 used as an arsenic scavenger for *in situ* remediation of phosphate-rich groundwater
835 and soil.

ACKNOWLEDGEMENTS

836

837 This work was financially supported by the National Key Research and Development
838 Program of China (Grant No. 2017YFC0602306), the National Natural Science
839 Foundation of China (Grant Nos. 41773113 and 41825003), Natural Science
840 Foundation for Distinguished Young Scientists of Guangdong Province (Grant No.
841 2020B1515020015), Science and Technology Program of Guangzhou, China (Grant
842 No. 201804020037), and the Youth Innovation Promotion Association CAS (Grant No.
843 Y201863). D.S.-C. and N.H.d.L. acknowledge the Engineering and Physical Sciences
844 Research Council (EPSRC, Grant No. EP/K009567) for funding. *Via* our membership
845 of the UK's HEC Materials Chemistry Consortium, which is funded by EPSRC (Grant
846 No. EP/L000202 and EP/R029431), this work used the ARCHER UK National
847 Supercomputing Service (<http://www.archer.ac.uk>). This work also used the
848 computational facilities of the Advanced Research Computing @ Cardiff (ARCCA)
849 Division, Cardiff University. This research was undertaken using the Supercomputing
850 Facilities at Cardiff University operated by ARCCA on behalf of the Cardiff
851 Supercomputing Facility, HPC Wales and Supercomputing Wales (SCW) projects. We
852 acknowledge the support of the latter, which is part-funded by the European Regional
853 Development Fund (ERDF) *via* Welsh Government. All data created during this
854 research is openly available from the Cardiff University's Research Portal at
855 <http://doi.org/10.17035/d.2019.0081529534>.

856 **Appendix A. Supplementary material**

857 Supplementary data associated with this article can be found in the online version, at

858 XXX.

REFERENCES CITED

859

860 Anisimov, V.I., Korotin, M.A., Zaanen, J., and Andersen, O.K. (1992) Spin Bags,
861 Polarons, and Impurity Potentials in $\text{La}_{2-x}\text{Sr}_x\text{CuO}_4$ from 1st Principles.
862 Physical Review Letters, 68(3), 345-348.

863 Antelo, J., Arce, F., and Fiol, S. (2015) Arsenate and phosphate adsorption on
864 ferrihydrite nanoparticles. Synergetic interaction with calcium ions. Chemical
865 Geology, 410, 53-62.

866 Arai, Y., and Sparks, D.L. (2001) ATR-FTIR spectroscopic investigation on
867 phosphate adsorption mechanisms at the ferrihydrite-water interface. Journal
868 of Colloid and Interface Science, 241(2), 317-326.

869 Blochl, P.E. (1994) Projector Augmented-Wave Method. Physical Review B, 50(24),
870 17953-17979.

871 Brechbuhl, Y., Christl, I., Elzinga, E.J., and Kretzschmar, R. (2012) Competitive
872 sorption of carbonate and arsenic to hematite: Combined ATR-FTIR and batch
873 experiments. Journal of Colloid and Interface Science, 377, 313-321.

874 Carabante, I., Grahn, M., Holmgren, A., and Hedlund, J. (2010) In situ ATR-FTIR
875 studies on the competitive adsorption of arsenate and phosphate on ferrihydrite.
876 Journal of Colloid and Interface Science, 351(2), 523-531.

877 Carabante, I., Grahn, M., Holmgren, A., Kumpiene, J., and Hedlund, J. (2009)
878 Adsorption of As (V) on iron oxide nanoparticle films studied by in situ
879 ATR-FTIR spectroscopy. Colloids and Surfaces a-Physicochemical and
880 Engineering Aspects, 346(1-3), 106-113.

- 881 Catalano, J.G., Park, C., Fenter, P., and Zhang, Z. (2008) Simultaneous inner- and
882 outer-sphere arsenate adsorption on corundum and hematite. *Geochimica Et*
883 *Cosmochimica Acta*, 72(8), 1986-2004.
- 884 Chakraborti, D., Rahman, M.M., Paul, K., Chowdhury, U.K., Sengupta, M.K., Lodh,
885 D., Chanda, C.R., Saha, K.C., and Mukherjee, S.C. (2002) Arsenic calamity in
886 the Indian subcontinent - What lessons have been learned? *Talanta*, 58(1),
887 3-22.
- 888 Choppala, G., Bolan, N., Kunhikrishnan, A., and Bush, R. (2016) Differential effect
889 of biochar upon reduction-induced mobility and bioavailability of arsenate and
890 chromate. *Chemosphere*, 144, 374-381.
- 891 Correll, D.L. (1998) The role of phosphorus in the eutrophication of receiving waters:
892 A review. *Journal of Environmental Quality*, 27(2), 261-266.
- 893 Dudarev, S.L., Botton, G.A., Savrasov, S.Y., Humphreys, C.J., and Sutton, A.P.
894 (1998) Electron-energy-loss spectra and the structural stability of nickel oxide:
895 An LSDA+U study. *Physical Review B*, 57(3), 1505-1509.
- 896 Dupuis, C., and Beaudoin, G. (2011) Discriminant diagrams for iron oxide trace
897 element fingerprinting of mineral deposit types. *Mineralium Deposita*, 46(4),
898 319-335.
- 899 Elzinga, E.J., and Sparks, D.L. (2007) Phosphate adsorption onto hematite: An in situ
900 ATR-FTIR investigation of the effects of pH and loading level on the mode of
901 phosphate surface complexation. *Journal of Colloid and Interface Science*,
902 308(1), 53-70.

- 903 Fendorf, S., Eick, M.J., Grossl, P., and Sparks, D.L. (1997) Arsenate and chromate
904 retention mechanisms on goethite .1. Surface structure. Environmental Science
905 & Technology, 31(2), 315-320.
- 906 Filip, J., Karlicky, F., Marusak, Z., Lazar, P., Cernik, M., Otyepka, M., and Zboril, R.
907 (2014) Anaerobic reaction of nanoscale zerovalent iron with water:
908 Mechanism and kinetics. Journal of Physical Chemistry C, 118(25),
909 13817-13825.
- 910 Gao, X.D., Root, R.A., Farrell, J., Ela, W., and Chorover, J. (2013) Effect of silicic
911 acid on arsenate and arsenite retention mechanisms on 6-L ferrihydrite: A
912 spectroscopic and batch adsorption approach. Applied Geochemistry, 38,
913 110-120.
- 914 Gao, Y., and Mucci, A. (2001) Acid base reactions, phosphate and arsenate
915 complexation, and their competitive adsorption at the surface of goethite in 0.7
916 M NaCl solution. Geochimica Et Cosmochimica Acta, 65(14), 2361-2378.
- 917 Gorski, C.A., Nurmi, J.T., Tratnyek, P.G., Hofstetter, T.B., and Scherer, M.M. (2010)
918 Redox behavior of magnetite: Implications for contaminant reduction.
919 Environmental Science & Technology, 44(1), 55-60.
- 920 Grimme, S. (2006) Semiempirical GGA-type density functional constructed with a
921 long-range dispersion correction. Journal of Computational Chemistry, 27(15),
922 1787-1799.
- 923 Grossl, P.R., Eick, M., Sparks, D.L., Goldberg, S., and Ainsworth, C.C. (1997)
924 Arsenate and chromate retention mechanisms on goethite .2. Kinetic

- 925 evaluation using a pressure-jump relaxation technique. *Environmental Science*
926 & *Technology*, 31(2), 321-326.
- 927 Guo, H.B., and Barnard, A.S. (2013) Naturally occurring iron oxide nanoparticles:
928 morphology, surface chemistry and environmental stability. *Journal of*
929 *Materials Chemistry A*, 1(1), 27-42.
- 930 Han, J., and Ro, H.M. (2018) Interpreting competitive adsorption of arsenate and
931 phosphate on nanosized iron (hydr)oxides: effects of pH and surface loading.
932 *Environmental Science and Pollution Research*, 25(28), 28572-28582.
- 933 Hashem, M.A., Toda, K., and Ohira, S.I. (2015) Leaching behavior of arsenite and
934 arsenate from the contaminated sediment by the effect of phosphate ion under
935 anaerobic conditions. *Environmental Earth Sciences*, 74(1), 745-745.
- 936 He, G.Z., Zhang, M.Y., and Pan, G. (2009) Influence of pH on initial concentration
937 effect of arsenate adsorption on TiO₂ surfaces: Thermodynamic, DFT, and
938 EXAFS interpretations. *Journal of Physical Chemistry C*, 113(52),
939 21679-21686.
- 940 Hiemstra, T. (2013) Surface and mineral structure of ferrihydrite. *Geochimica Et*
941 *Cosmochimica Acta*, 105, 316-325.
- 942 Hingston, F.J., Posner, A.M., and Quirk, J.P. (1971) Competitive adsorption of
943 negatively charged ligands on oxide surfaces. *Discussions of the Faraday*
944 *Society*, 52(0), 334-342.
- 945 Hu, S., Yan, W., and Duan, J.M. (2015) Polymerization of silicate on TiO₂ and its
946 influence on arsenate adsorption: An ATR-FTIR study. *Colloids and Surfaces*

- 947 a-Physicochemical and Engineering Aspects, 469, 180-186.
- 948 Hug, S.J. (1997) In situ Fourier transform infrared measurements of sulfate adsorption
949 on hematite in aqueous solutions. *Journal of Colloid and Interface Science*,
950 188(2), 415-422.
- 951 Jia, Y.F., Xu, L.Y., Wang, X., and Demopoulos, G.P. (2007) Infrared spectroscopic
952 and X-ray diffraction characterization of the nature of adsorbed arsenate on
953 ferrihydrite. *Geochimica Et Cosmochimica Acta*, 71(7), 1643-1654.
- 954 Johnston, C.P., and Chrysochoou, M. (2012) Investigation of chromate coordination
955 on ferrihydrite by in situ ATR-FTIR spectroscopy and theoretical frequency
956 calculations. *Environmental Science & Technology*, 46(11), 5851-5858.
- 957 -. (2014) Mechanisms of chromate adsorption on hematite. *Geochimica Et*
958 *Cosmochimica Acta*, 138, 146-157.
- 959 Jonsson, J., and Sherman, D.M. (2008) Sorption of As(III) and As(V) to siderite,
960 green rust (fougerite) and magnetite: Implications for arsenic release in anoxic
961 groundwaters. *Chemical Geology*, 255(1-2), 173-181.
- 962 Kanematsu, M., Young, T.M., Fukushi, K., Green, P.G., and Darby, J.L. (2010)
963 Extended Triple Layer Modeling of Arsenate and Phosphate Adsorption on a
964 Goethite-based Granular Porous Adsorbent. *Environmental Science &*
965 *Technology*, 44(9), 3388-3394.
- 966 Kocourkova-Vikova, E., Loun, J., Sracek, O., Houzar, S., and Filip, J. (2015)
967 Secondary arsenic minerals and arsenic mobility in a historical waste rock pile
968 at Kank near Kutna Hora, Czech Republic. *Mineralogy and Petrology*, 109(1),

- 969 17-33.
- 970 Kresse, G., and Furthmuller, J. (1996a) Efficiency of ab-initio total energy
971 calculations for metals and semiconductors using a plane-wave basis set.
972 Computational Materials Science, 6(1), 15-50.
- 973 -. (1996b) Efficient iterative schemes for ab initio total-energy calculations using a
974 plane-wave basis set. Physical Review B, 54(16), 11169-11186.
- 975 Kresse, G., and Hafner, J. (1993) Abinitio Molecular-Dynamics for Liquid-Metals.
976 Physical Review B, 47(1), 558-561.
- 977 -. (1994) Ab-Initio Molecular-Dynamics Simulation of the Liquid-Metal
978 Amorphous-Semiconductor Transition in Germanium. Physical Review B,
979 49(20), 14251-14269.
- 980 Kresse, G., and Joubert, D. (1999) From ultrasoft pseudopotentials to the projector
981 augmented-wave method. Physical Review B, 59(3), 1758-1775.
- 982 Krumina, L., Kenney, J.P.L., Loring, J.S., and Persson, P. (2016) Desorption
983 mechanisms of phosphate from ferrihydrite and goethite surfaces. Chemical
984 Geology, 427, 54-64.
- 985 Kubicki, J.D., Paul, K.W., Kabalan, L., Zhu, Q., Mrozik, M.K., Aryanpour, M.,
986 Pierre-Louis, A.M., and Strongin, D.R. (2012) ATR-FTIR and density
987 functional theory study of the structures, energetics, and vibrational spectra of
988 phosphate adsorbed onto goethite. Langmuir, 28(41), 14573-14587.
- 989 Kunhikrishnan, A., Choppala, G., Seshadri, B., Wijesekara, H., Bolan, N.S., Mbene,
990 K., and Kim, W.-I. (2017) Impact of wastewater derived dissolved organic

- 991 carbon on reduction, mobility, and bioavailability of As (V) and Cr (VI) in
992 contaminated soils. *Journal of Environmental Management*, 186(2), 183-191.
- 993 Liang, X.L., Wei, G.L., Xiong, J., Tan, F.D., He, H.P., Qu, C.C., Yin, H., Zhu, J.X.,
994 Zhu, R.L., Qin, Z.H., and Zhang, J. (2017) Adsorption isotherm, mechanism,
995 and geometry of Pb(II) on magnetites substituted with transition metals.
996 *Chemical Geology*, 470, 132-140.
- 997 Liang, X.L., Zhong, Y.H., He, H.P., Yuan, P., Zhu, J.X., Zhu, S.Y., and Jiang, Z.
998 (2012) The application of chromium substituted magnetite as heterogeneous
999 Fenton catalyst for the degradation of aqueous cationic and anionic dyes.
1000 *Chemical Engineering Journal*, 191, 177-184.
- 1001 Liang, X.L., Zhong, Y.H., Zhu, S.Y., He, H.P., Yuan, P., Zhu, J.X., and Jiang, Z.
1002 (2013) The valence and site occupancy of substituting metals in magnetite
1003 spinel structure $Fe_{3-x}M_xO_4$ (M = Cr, Mn, Co and Ni) and their influence on
1004 thermal stability: An XANES and TG-DSC investigation. *Solid State Sciences*,
1005 15, 115-122.
- 1006 Liu, C.H., Chuang, Y.H., Chen, T.Y., Tian, Y., Li, H., Wang, M.K., and Zhang, W.
1007 (2015) Mechanism of arsenic adsorption on magnetite nanoparticles from
1008 water: Thermodynamic and spectroscopic Studies. *Environmental Science &*
1009 *Technology*, 49(m13), 7726-7734.
- 1010 Liu, F., De Cristofaro, A., and Violante, A. (2001) Effect of pH, phosphate and
1011 oxalate on the adsorption/desorption of arsenate on/from goethite. *Soil Science*,
1012 166(3), 197-208.

- 1013 Livi, K.J.T., Villalobos, M., Leary, R., Varela, M., Barnard, J., Villacis-Garcia, M.,
1014 Zanella, R., Goodridge, A., and Midgley, P. (2017) Crystal Face Distributions
1015 and Surface Site Densities of Two Synthetic Goethites: Implications for
1016 Adsorption Capacities as a Function of Particle Size. *Langmuir*, 33(36),
1017 8924-8932.
- 1018 Loring, J.S., Sandstrom, M.H., Noren, K., and Persson, P. (2009) Rethinking arsenate
1019 coordination at the surface of goethite. *Chemistry-a European Journal*, 15(20),
1020 5063-5072.
- 1021 Luengo, C., Brigante, M., Antelo, J., and Avena, M. (2006) Kinetics of phosphate
1022 adsorption on goethite: Comparing batch adsorption and ATR-IR
1023 measurements. *Journal of Colloid and Interface Science*, 300(2), 511-518.
- 1024 Lumsdon, D.G., Fraser, A.R., Russell, J.D., and Livesey, N.T. (1984) New infrared
1025 band assignments for the arsenate ion adsorbed on synthetic goethite
1026 (α -FeOOH). *Journal of Soil Science*, 35(3), 381-386.
- 1027 Manning, B.A., and Goldberg, S. (1996) Modeling competitive adsorption of arsenate
1028 with phosphate and molybdate on oxide minerals. *Soil Science Society of
1029 America Journal*, 60, 121-131.
- 1030 Melamed, R., Jurinak, J.J., and Dudley, L.M. (1995) Effect of adsorbed phosphate on
1031 transport of arsenate through an oxisol. *Soil Science Society of America
1032 Journal*, 59(5), 1289-1294.
- 1033 Mermin, D.N. (1965) Thermal properties of the inhomogeneous electron gas. *Physical
1034 Review*, 137(5A), A1441-A1443.

- 1035 Mohan, D., and Pittman, C.U. (2007) Arsenic removal from water/wastewater using
1036 adsorbents - A critical review. *Journal of Hazardous Materials*, 142(1-2), 1-53.
- 1037 Neel, L. (1948) Proprietes Magnetiques Des Ferrites - Ferrimagnetisme Et
1038 Antiferromagnetisme. *Annales De Physique*, 3(2), 137-198.
- 1039 Neupane, G., Donahoe, R.J., and Arai, Y. (2014) Kinetics of competitive
1040 adsorption/desorption of arsenate and phosphate at the ferrihydrite-water
1041 interface. *Chemical Geology*, 368, 31-38.
- 1042 O'Reilly, S.E., Strawn, D.G., and Sparks, D.L. (2001) Residence time effects on
1043 arsenate adsorption/desorption mechanisms on goethite. *Soil Science Society
1044 of America Journal*, 65(1), 67-77.
- 1045 Ona-Nguema, G., Morin, G., Juillot, F., Calas, G., and Brown, G.E. (2005) EXAFS
1046 analysis of arsenite adsorption onto two-line ferrihydrite, hematite, goethite,
1047 and lepidocrocite. *Environmental Science & Technology*, 39(23), 9147-9155.
- 1048 Pathak, A.K., and Bandyopadhyay, T. (2016) Solvation of arsenate anion: combined
1049 quantum mechanics and molecular dynamics based investigation. *Molecular
1050 Physics*, 114(13), 2029-2036.
- 1051 Pedersen, H.D., Postma, D., Jakobsen, R., and Larsen, O. (2005) Fast transformation
1052 of iron oxyhydroxides by the catalytic action of aqueous Fe(II). *Geochimica Et
1053 Cosmochimica Acta*, 69(16), 3967-3977.
- 1054 Perdew, J.P., Burke, K., and Ernzerhof, M. (1996) Generalized gradient
1055 approximation made simple. *Physical Review Letters*, 77(18), 3865-3868.
- 1056 -. (1997) Generalized gradient approximation made simple (vol 77, pg 3865, 1996).

- 1057 Physical Review Letters, 78(7), 1396-1396.
- 1058 Peryea, F.J. (1991) Phosphate-induced release of arsenic from soils contaminated with
1059 lead arsenate. Soil Science Society of America Journal, 55(5), 1301-1306.
- 1060 Sabur, M.A., Goldberg, S., Gale, A., Kabengi, N., and Al-Abadleh, H.A. (2015)
1061 Temperature-Dependent Infrared and Calorimetric Studies on Arsenicals
1062 Adsorption from Solution to Hematite Nanoparticles. Langmuir, 31(9),
1063 2749-2760.
- 1064 Santos-Carballal, D., Roldan, A., Dzade, N.Y., and de Leeuw, N.H. (2018) Reactivity
1065 of CO₂ on the surfaces of magnetite (Fe₃O₄), greigite (Fe₃S₄) and mackinawite
1066 (FeS). Philosophical Transactions of the Royal Society a-Mathematical
1067 Physical and Engineering Sciences, 376(2110).
- 1068 Santos-Carballal, D., Roldan, A., Grau-Crespo, R., and de Leeuw, N.H. (2014) A
1069 DFT study of the structures, stabilities and redox behaviour of the major
1070 surfaces of magnetite Fe₃O₄. Physical Chemistry Chemical Physics, 16(39),
1071 21082-21097.
- 1072 Scott, T.B., Allen, G.C., Heard, P.J., and Randell, M.G. (2005) Reduction of U(VI) to
1073 U(IV) on the surface of magnetite. Geochimica Et Cosmochimica Acta, 69(24),
1074 5639-5646.
- 1075 Sherman, D.M., and Randall, S.R. (2003) Surface complexation of arsenic(V) to
1076 iron(III) (hydr)oxides: Structural mechanism from ab initio molecular
1077 geometries and EXAFS spectroscopy. Geochimica Et Cosmochimica Acta,
1078 67(22), 4223-4230.

- 1079 Shull, C.G., Wollan, E.O., and Koehler, W.C. (1951) Neutron Scattering and
1080 Polarization by Ferromagnetic Materials. *Physical Review*, 84(5), 912-921.
- 1081 Silva, and Fraustoda, J.R.R. (2001) The biological chemistry of the elements : the
1082 inorganic chemistry of life. 62-63 p. Clarendon Press.
- 1083 So, H.U., Postma, D., Jakobsen, R., and Larsen, F. (2012) Competitive adsorption of
1084 arsenate and phosphate onto calcite; experimental results and modeling with
1085 CCM and CD-MUSIC. *Geochimica Et Cosmochimica Acta*, 93, 1-13.
- 1086 Sprague, D.D., and Vermaire, J.C. (2018) Legacy Arsenic Pollution of Lakes Near
1087 Cobalt, Ontario, Canada: Arsenic in Lake Water and Sediment Remains
1088 Elevated Nearly a Century After Mining Activity Has Ceased. *Water Air and
1089 Soil Pollution*, 229(3).
- 1090 Sun, Z.X., Su, F.W., Forsling, W., and Samskog, P.O. (1998) Surface characteristics
1091 of magnetite in aqueous suspension. *Journal of Colloid and Interface Science*,
1092 197(1), 151-159.
- 1093 Swedlund, P.J., Holtkamp, H., Song, Y.T., and Daughney, C.J. (2014)
1094 Arsenate-ferrihydrite systems from minutes to months: A macroscopic and IR
1095 spectroscopic study of an elusive equilibrium. *Environmental Science &
1096 Technology*, 48(5), 2759-2765.
- 1097 Tamura, H., Katayama, N., and Furuichi, R. (1993) Modeling the ion-exchange
1098 adsorption of heavy-metal ions on the surface of metal-oxides. *Bunseki
1099 Kagaku*, 42(11), 719-724.
- 1100 Tejedortejedor, M.I., and Anderson, M.A. (1990) Protonation of phosphate on the

- 1101 surface of goethite as studied by cir-FTIR and electrophoretic mobility.
1102 Langmuir, 6(3), 602-611.
- 1103 Tiberg, C., Sjostedt, C., Persson, I., and Gustafsson, J.P. (2013) Phosphate effects on
1104 copper(II) and lead(II) sorption to ferrihydrite. *Geochimica Et Cosmochimica*
1105 *Acta*, 120, 140-157.
- 1106 Villalobos, M., Cheney, M.A., and Alcaraz-Cienfuegos, J. (2009) Goethite surface
1107 reactivity: II. A microscopic site-density model that describes its surface
1108 area-normalized variability. *Journal of Colloid and Interface Science*, 336(2),
1109 412-422.
- 1110 Violante, A., and Pigna, M. (2002) Competitive sorption of arsenate and phosphate on
1111 different clay minerals and soils. *Soil Science Society of America Journal*,
1112 66(6), 1788-1796.
- 1113 WHO. (2011) *Guidelines for Drinking-water Quality* 4th Ed.
- 1114 Winkel, L.H.E., Pham, T.K.T., Vi, M.L., Stengel, C., Amini, M., Nguyen, T.H., Pham,
1115 H.V., and Berg, M. (2011) Arsenic pollution of groundwater in Vietnam
1116 exacerbated by deep aquifer exploitation for more than a century. *Proceedings*
1117 *of the National Academy of Sciences of the United States of America*, 108(4),
1118 1246-1251.
- 1119 Xu, R.K., Kozak, L.M., and Huang, P.M. (2008) Kinetics of phosphate-induced
1120 desorption of arsenate adsorbed on crystalline and amorphous aluminum
1121 hydroxides. *Soil Science*, 173(10), 683-693.
- 1122 Yan, W., Wang, H.B., and Jing, C.Y. (2016) Adhesion of *Shewanella oneidensis*

- 1123 MR-1 to Goethite: A Two-Dimensional Correlation Spectroscopic Study.
1124 Environmental Science & Technology, 50(8), 4343-4349.
- 1125 Zhang, J.H., Zhang, C.H., Wei, G.L., Li, Y., Liang, X.L., Chu, W., He, H.P., Huang,
1126 D.Y., Zhu, J.X., and Zhu, R.L. (2017a) Reduction removal of hexavalent
1127 chromium by zinc-substituted magnetite coupled with aqueous Fe(II) at
1128 neutral pH value. Journal of Colloid and Interface Science, 500, 20-29.
- 1129 Zhang, L., Qin, X., Tang, J., Liu, W., and Yang, H. (2017b) Review of arsenic
1130 geochemical characteristics and its significance on arsenic pollution studies in
1131 karst groundwater, Southwest China. Applied Geochemistry, 77, 80-88.
- 1132 Zhang, M.Y., Pan, G., Zhao, D.Y., and He, G.Z. (2011) XAFS study of
1133 starch-stabilized magnetite nanoparticles and surface speciation of arsenate.
1134 Environmental Pollution, 159(12), 3509-3514.
- 1135 Zhao, H.S., and Stanforth, R. (2001) Competitive adsorption of phosphate and
1136 arsenate on goethite. Environmental Science & Technology, 35(24),
1137 4753-4757.
- 1138 Zhao, L.J., Zhang, H.J., Xing, Y., Song, S.Y., Yu, S.Y., Shi, W.D., Guo, X.M., Yang,
1139 H.H., Le, Y.Q., and Cao, F. (2008) Morphology-controlled synthesis of
1140 magnetites with nanoporous structures and excellent magnetic properties.
1141 Chemistry of Materials, 20(1), 198-204.
- 1142
- 1143

1144

TABLES

1145 **TABLE 1.** Adsorption sites, mean interatomic distances (d) and bond angles (\angle) for the energetically preferred outer- (OS) and inner-sphere (IS)

1146 complexes of arsenate and phosphate at the Fe₃O₄ (001) surface in both acid and alkaline conditions.

Solute	pH	Adsorption site	^a $d(X-O)$	$d(X=O)$	$d(XO-H)$	$d(XO-Fe)$	$d(Fe-OH)$	$d(FeO-H)$	$\angle(O-X-O)$	$\angle(O-X=O)$	$\angle(O=X=O)$	$\angle(XOH)$
			(Å)							(°)		
H ₂ AsO ₄ ⁻	acid	–	1.77	1.69	1.04	–	–	–	104.72	108.90	116.03	108.08
HAsO ₄		Fe _B , Fe _B	1.76	1.72	1.05	2.06		1.02	–	107.31	111.54	112.97
HAsO ₄ ²⁻	alkaline	–	1.76	1.72	1.01	–	1.92	0.99	–	109.81	109.06	109.42
HAsO ₄		Fe _B , Fe _B	1.82	1.71	1.01	2.00	2.00	0.99	–	104.45	114.00	106.64
H ₂ PO ₄ ⁻	acid	–	1.60	1.53	1.02	–	–	–	105.88	109.06	114.38	114.21
HPO ₄		Fe _B	1.65	1.54	0.98	2.08	–	0.98	–	105.01	113.55	114.25
HPO ₄ ²⁻	alkaline	–	1.60	1.54	1.03	–	1.95	0.97	–	106.99	111.87	120.38
PO ₄		Fe _A , Fe _B	–	1.56	–	1.93	–	–	–	–	109.44	–

1147 ^a: X represents the central atom (P or As) of adsorbate.

1148 **TABLE 2.** Adsorption sites, adsorption energies (E_{ads}) and charges (q) for the energetically preferred outer- (OS) and inner-sphere (IS)
 1149 complexes of arsenate and phosphate at the Fe_3O_4 (001) surface in both acid and alkaline conditions.

Solute	pH	Adsorption site	E_{ads} (eV per molecule)	${}^a q(\text{H}_m\text{XO}_4)$ (e^-)	$q(\text{OH})$	$q(\text{H})$
H_2AsO_4^-	acid	–	–	–0.82	–	–
HAsO_4		Fe_B, Fe_B	–2.19	–1.42	–	0.67
HAsO_4^{2-}	alkaline	–	–	–1.52	–0.66	–
HAsO_4		Fe_B, Fe_B	–0.84	–1.38	–0.68	–
H_2PO_4^-	acid	–	–	–0.84	–	–
HPO_4		Fe_B	–1.89	–1.50	–	0.65
HPO_4^{2-}	alkaline	–	–	–1.54	–0.65	–
PO_4		Fe_A, Fe_B	–0.69	–2.13	–	–

1150 ^a: X represents the central atom (P or As) of adsorbate. m indicates the degree of protonation of the solute, which can take integer values from 0 to 3.

1151

1152 **TABLE 3.** Molecular point groups, adsorption sites and wavenumbers of the fundamental vibrational modes for the energetically preferred
 1153 outer- (OS) and inner-sphere (IS) complexes of arsenate and phosphate at the Fe₃O₄ (001) surface in both acid and alkaline conditions. The
 1154 presented vibrational frequencies are stretching (ν), bending (δ) and wagging (ω).

Solute	pH	Sym	Adsorption site	$\nu(\text{FeO-H})$ (cm ⁻¹)	^a $\nu(\text{XO-H})$	$\delta(\text{XOH})$	$\omega(\text{XOH})$	$\nu(\text{X=O})$	$\nu(\text{X-OH})$	$\nu(\text{X=OFe})$	$\delta(\text{FeOH})$	$\omega(\text{FeOH})$
H ₂ AsO ₄ ⁻	acid	C _{2v}	OS	–	3066	1372	1028	870	735	–	–	–
					2266	1268	756	817	666			
HAsO ₄ ²⁻		C _s	Fe _B , Fe _B	2875	2429	1291	1037	816	721	786	1042	1035
										751		
HAsO ₄ ²⁻	alkaline	C _{3v}	OS	3365	3120	1190	776	830	728	–	1060	721
								790				
								756				
HAsO ₄ ²⁻		C _s	Fe _B , Fe _B	3458	3007	1278	830	792	624	810	928	797
										782		
H ₂ PO ₄ ⁻	acid	C _{2v}	OS	–	2826	1269	938	1096	904	–	–	–
					2742	1221	920	1012	839			
HPO ₄ ²⁻		C _s	Fe _B	3350	3625	1018	–	1088	766	942	1170	706
								1045				
HPO ₄ ²⁻	alkaline	C _{3v}	OS	3739	2626	1271	947	1045	867	–	718	616
								1003				
								926				
PO ₄ ³⁻		C _s	Fe _A , Fe _B	–	–	–	–	1112	–	909	–	–
								949		884		

1155 ^a: X represents the central atom (P or As) of adsorbate.

FIGURE CAPTIONS

1156

1157 **FIGURE 1.** Infrared spectra for the individual adsorption of arsenate (a) and
1158 phosphate (b) on magnetite surface at acid, neutral and alkaline conditions, as well as
1159 the spectral fitting with different adsorption species (arsenate: inner-sphere (green
1160 line) and outer-sphere (red line) species; phosphate: monoprotonated
1161 monodentate-mononuclear (green line) and non-protonated bidentate-binuclear
1162 complexes (red line)). The total fit is represented by the blue line.

1163

1164 **FIGURE 2.** Integrated absorbance (IA) of the bands assigned to the adsorbed
1165 arsenate (a) and phosphate (b) plotted vs. pH, and the relative percentage of different
1166 adsorption species (arsenate: inner-sphere and outer-sphere species; phosphate:
1167 monoprotonated monodentate-mononuclear (MMM) and non-protonated
1168 bidentate-binuclear (NBB) complexes).

1169

1170 **FIGURE 3.** Infrared spectra of phosphate adsorbed onto magnetite at pH = 4 (a), pH
1171 = 7 (b) and pH = 9 (c). After 135 (a and b) or 350 (c) min, arsenate was added at an
1172 equal (molar) concentration and the spectral change was monitored for another 135
1173 (a and b) or 350 (c) min.

1174

1175 **FIGURE 4.** Infrared spectra of arsenate adsorbed onto magnetite at pH = 4 (a) and
1176 pH = 7 (b). After 135 min, a phosphate solution at an equal (molar) concentration
1177 was added and the spectral change was monitored for another 135 (a and b) min.

1178

1179 **FIGURE 5.** Top and side view of the aqueous inner-sphere species HAsO_4^{2-} in (a)
1180 acid and (b) alkaline conditions. Tetrahedral Fe_A atoms are in orange, octahedral Fe_B
1181 atoms are in violet, O atoms are in red, As atoms are in green and H atoms are in
1182 pink. Surface atoms are represented as (top panels) balls and (bottom panels) sticks,
1183 water solvent molecules are represented as wireframe and the solute molecules are
1184 represented as balls-and-sticks. Light and dark dashed lines mark hydrogen bonds
1185 and the limits of the computational cell, respectively. The double arrows indicate
1186 interatomic distances in Å.

1187

1188 **FIGURE 6.** Top and side view of the aqueous inner-sphere species (a) HPO_4^{2-} and
1189 (b) PO_4^{3-} in acid and alkaline conditions, respectively. Tetrahedral Fe_A atoms are in
1190 orange, octahedral Fe_B atoms are in violet, O atoms are in red, P atoms are in blue
1191 and H atoms are in pink. Surface atoms are represented as (top panels) balls and
1192 (bottom panels) sticks, water solvent molecules are represented as wireframe and the
1193 solute molecules are represented as balls-and-sticks. Light and dark dashed lines
1194 mark hydrogen bonds and the limits of the computational cell, respectively. The
1195 double arrows indicate interatomic distances in Å.

1144

TABLES

1145 **TABLE 1.** Adsorption sites, mean interatomic distances (d) and bond angles (\angle) for the energetically preferred outer- (OS) and inner-sphere (IS)
 1146 complexes of arsenate and phosphate at the Fe₃O₄ (001) surface in both acid and alkaline conditions.

Solute	pH	Adsorption site	^a $d(X-O)$	$d(X=O)$	$d(XO-H)$	$d(XO-Fe)$	$d(Fe-OH)$	$d(FeO-H)$	$\angle(O-X-O)$	$\angle(O-X=O)$	$\angle(O=X=O)$	$\angle(XOH)$
			(Å)								(°)	
H ₂ AsO ₄ ⁻	acid	–	1.77	1.69	1.04	–	–	–	104.72	108.90	116.03	108.08
HAsO ₄		Fe _B , Fe _B	1.76	1.72	1.05	2.06		1.02	–	107.31	111.54	112.97
HAsO ₄ ²⁻	alkaline	–	1.76	1.72	1.01	–	1.92	0.99	–	109.81	109.06	109.42
HAsO ₄		Fe _B , Fe _B	1.82	1.71	1.01	2.00	2.00	0.99	–	104.45	114.00	106.64
H ₂ PO ₄ ⁻	acid	–	1.60	1.53	1.02	–	–	–	105.88	109.06	114.38	114.21
HPO ₄		Fe _B	1.65	1.54	0.98	2.08	–	0.98	–	105.01	113.55	114.25
HPO ₄ ²⁻	alkaline	–	1.60	1.54	1.03	–	1.95	0.97	–	106.99	111.87	120.38
PO ₄		Fe _A , Fe _B	–	1.56	–	1.93	–	–	–	–	109.44	–

1147 ^a: X represents the central atom (P or As) of adsorbate.

1148 **TABLE 2.** Adsorption sites, adsorption energies (E_{ads}) and charges (q) for the energetically preferred outer- (OS) and inner-sphere (IS)
 1149 complexes of arsenate and phosphate at the Fe_3O_4 (001) surface in both acid and alkaline conditions.

Solute	pH	Adsorption site	E_{ads} (eV per molecule)	${}^a q(\text{H}_m\text{XO}_4)$ (e^-)	$q(\text{OH})$	$q(\text{H})$
H_2AsO_4^-	acid	–	–	–0.82	–	–
HAsO_4		Fe_B, Fe_B	–2.19	–1.42	–	0.67
HAsO_4^{2-}	alkaline	–	–	–1.52	–0.66	–
HAsO_4		Fe_B, Fe_B	–0.84	–1.38	–0.68	–
H_2PO_4^-	acid	–	–	–0.84	–	–
HPO_4		Fe_B	–1.89	–1.50	–	0.65
HPO_4^{2-}	alkaline	–	–	–1.54	–0.65	–
PO_4		Fe_A, Fe_B	–0.69	–2.13	–	–

1150 ^a: X represents the central atom (P or As) of adsorbate. m indicates the degree of protonation of the solute, which can take integer values from 0 to 3.

1151

1152 **TABLE 3.** Molecular point groups, adsorption sites and wavenumbers of the fundamental vibrational modes for the energetically preferred
 1153 outer- (OS) and inner-sphere (IS) complexes of arsenate and phosphate at the Fe₃O₄ (001) surface in both acid and alkaline conditions. The
 1154 presented vibrational frequencies are stretching (ν), bending (δ) and wagging (ω).

Solute	pH	Sym	Adsorption site	$\nu(\text{FeO-H})$ (cm ⁻¹)	^a $\nu(\text{XO-H})$	$\delta(\text{XOH})$	$\omega(\text{XOH})$	$\nu(\text{X=O})$	$\nu(\text{X-OH})$	$\nu(\text{X=OFe})$	$\delta(\text{FeOH})$	$\omega(\text{FeOH})$
H ₂ AsO ₄ ⁻	acid	C _{2v}	OS	–	3066	1372	1028	870	735	–	–	–
					2266	1268	756	817	666			
HAsO ₄ ²⁻		C _s	Fe _B , Fe _B	2875	2429	1291	1037	816	721	786	1042	1035
										751		
HAsO ₄ ²⁻	alkaline	C _{3v}	OS	3365	3120	1190	776	830	728	–	1060	721
								790				
								756				
HAsO ₄ ²⁻		C _s	Fe _B , Fe _B	3458	3007	1278	830	792	624	810	928	797
										782		
H ₂ PO ₄ ⁻	acid	C _{2v}	OS	–	2826	1269	938	1096	904	–	–	–
					2742	1221	920	1012	839			
HPO ₄ ²⁻		C _s	Fe _B	3350	3625	1018	–	1088	766	942	1170	706
								1045				
HPO ₄ ²⁻	alkaline	C _{3v}	OS	3739	2626	1271	947	1045	867	–	718	616
								1003				
								926				
PO ₄ ³⁻		C _s	Fe _A , Fe _B	–	–	–	–	1112	–	909	–	–
								949		884		

1155 ^a: X represents the central atom (P or As) of adsorbate.

FIGURE CAPTIONS

1156

1157 **FIGURE 1.** Infrared spectra for the individual adsorption of arsenate (a) and
1158 phosphate (b) on magnetite surface at acid, neutral and alkaline conditions, as well as
1159 the spectral fitting with different adsorption species (arsenate: inner-sphere (green
1160 line) and outer-sphere (red line) species; phosphate: monoprotonated
1161 monodentate-mononuclear (green line) and non-protonated bidentate-binuclear
1162 complexes (red line)). The total fit is represented by the blue line.

1163

1164 **FIGURE 2.** Integrated absorbance (IA) of the bands assigned to the adsorbed
1165 arsenate (a) and phosphate (b) plotted vs. pH, and the relative percentage of different
1166 adsorption species (arsenate: inner-sphere and outer-sphere species; phosphate:
1167 monoprotonated monodentate-mononuclear (MMM) and non-protonated
1168 bidentate-binuclear (NBB) complexes).

1169

1170 **FIGURE 3.** Infrared spectra of phosphate adsorbed onto magnetite at pH = 4 (a), pH
1171 = 7 (b) and pH = 9 (c). After 135 (a and b) or 350 (c) min, arsenate was added at an
1172 equal (molar) concentration and the spectral change was monitored for another 135
1173 (a and b) or 350 (c) min.

1174

1175 **FIGURE 4.** Infrared spectra of arsenate adsorbed onto magnetite at pH = 4 (a) and
1176 pH = 7 (b). After 135 min, a phosphate solution at an equal (molar) concentration
1177 was added and the spectral change was monitored for another 135 (a and b) min.

1178

1179 **FIGURE 5.** Top and side view of the aqueous inner-sphere species HAsO_4^{2-} in (a)
1180 acid and (b) alkaline conditions. Tetrahedral Fe_A atoms are in orange, octahedral Fe_B
1181 atoms are in violet, O atoms are in red, As atoms are in green and H atoms are in
1182 pink. Surface atoms are represented as (top panels) balls and (bottom panels) sticks,
1183 water solvent molecules are represented as wireframe and the solute molecules are
1184 represented as balls-and-sticks. Light and dark dashed lines mark hydrogen bonds
1185 and the limits of the computational cell, respectively. The double arrows indicate
1186 interatomic distances in Å.

1187

1188 **FIGURE 6.** Top and side view of the aqueous inner-sphere species (a) HPO_4^{2-} and
1189 (b) PO_4^{3-} in acid and alkaline conditions, respectively. Tetrahedral Fe_A atoms are in
1190 orange, octahedral Fe_B atoms are in violet, O atoms are in red, P atoms are in blue
1191 and H atoms are in pink. Surface atoms are represented as (top panels) balls and
1192 (bottom panels) sticks, water solvent molecules are represented as wireframe and the
1193 solute molecules are represented as balls-and-sticks. Light and dark dashed lines
1194 mark hydrogen bonds and the limits of the computational cell, respectively. The
1195 double arrows indicate interatomic distances in Å.

Figure.1

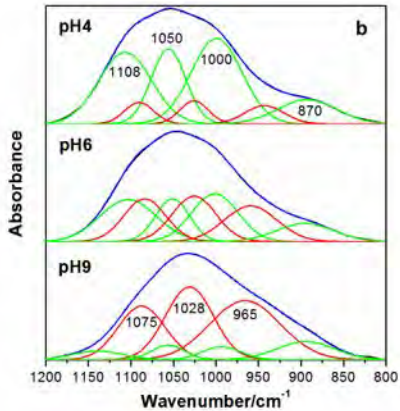
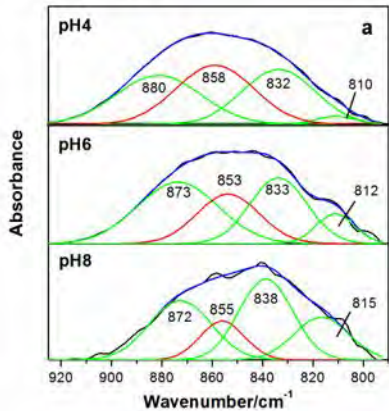


Figure.2

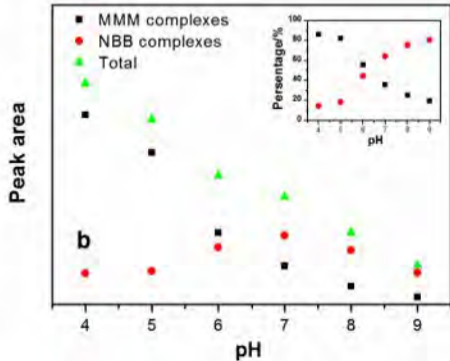
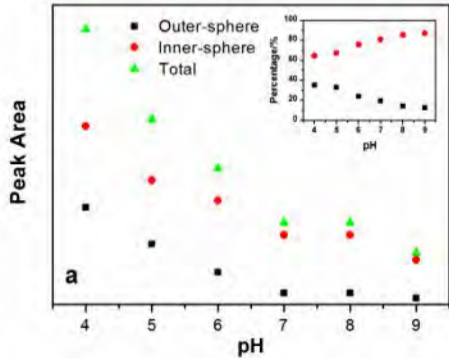


Figure.3

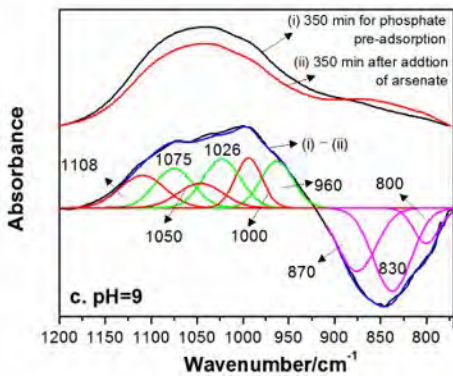
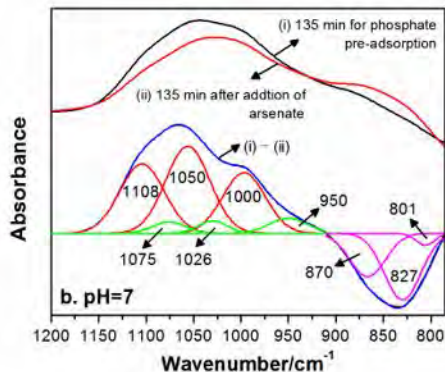
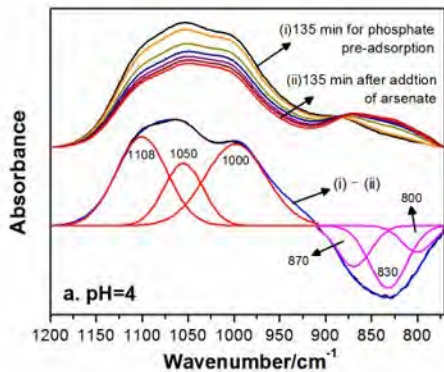


Figure.4

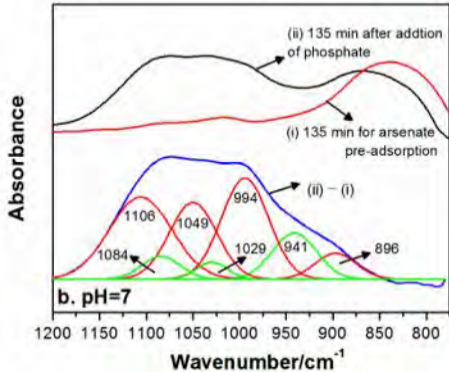
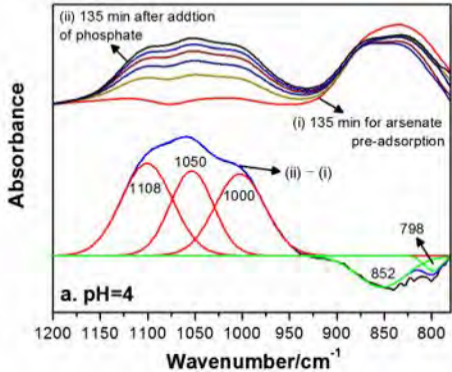


Figure.5.

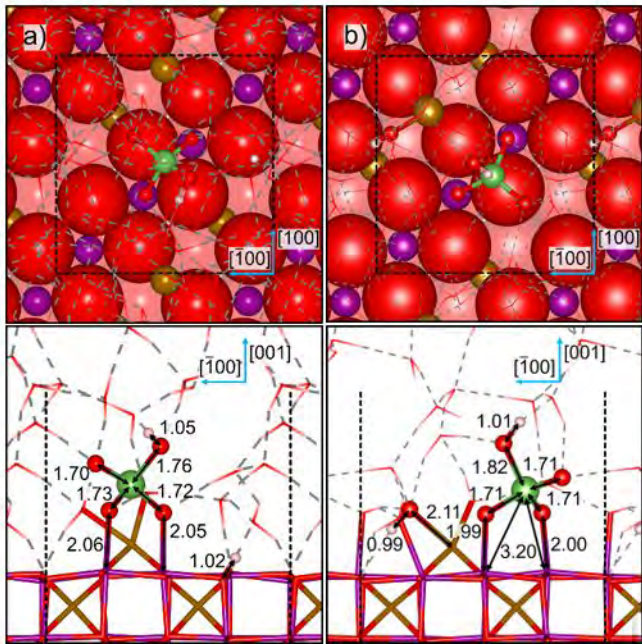


Figure.6

